



CHALMERS
UNIVERSITY OF TECHNOLOGY

Experimental heat transfer measurement technique validation and measurements in a linear cascade of an OGV and endwall

Master's Thesis in Solid and Fluid Mechanics

Carmen Urbiola Merina

Department of Applied Mechanics
Division of Fluid Dynamics
CHALMERS UNIVERSITY OF TECHNOLOGY
Göteborg Sweden, 2015

Master's Thesis [2015 : 66]

MASTER'S THESIS 2015:66

**Experimental heat transfer measurement technique
validation and measurements in a linear cascade of
an OGV and endwall.**

Master's Thesis

CARMEN URBIOLA MERINA

Department of Applied Mechanics
Division of Fluid Dynamics
CHALMERS UNIVERSITY OF TECHNOLOGY
Göteborg, Sweden, 2015

Experimental heat transfer measurement technique validation
and measurements in linear cascade of an OGV and endwall.

Master's Thesis

Carmen Urbiola Merina

© CARMEN URBIOLA MERINA, 2015

Master's Thesis 2015:66

ISSN: 1652-8557

Department of Applied Mechanics,
Division of Fluid Dynamics
Chalmers University of Technology
SE-412 96 Göteborg, Sweden
Phone +46-(0)31-7721400
Fax: +46-(0)31-180976

Printed at Chalmers Reproservice
Göteborg, Sweden 2015

Experimental heat transfer measurement technique validation and measurements in linear cascade of an OGV and endwall.

Master's Thesis

by

Carmen Urbiola Merina

urbiola@student.chalmers.se

Department of Applied Mechanics

Division of Fluid Dynamics

Chalmers University of Technology

Abstract

The scope of this Master thesis is to study the heat transfer on the endwall of an OGV located in a low speed linear cascade facility. Prior to performing these experiments, the instrumented endwall for heat transfer measurements was validated. Two experiments are carried out for this purpose. At first, a steady impinging jet over the instrumented endwall is studied while in the second experiment a flat plate case is studied. After the validation of the endwall the tests are performed in the linear cascade to evaluate the heat transfer coefficient of the OGV.

The heat transfer study performed on the endwall can help to understand better the complex heat transfer mechanisms involved in this case, and hence, the information can be used for CFD validation purposes. The OGVs are located downstream of the last stage of a low pressure turbine (LPT) where the exhaust gases are at high temperatures. Therefore, understanding of flow characteristics and heat transfer distribution in this hot structure has been of great interest of several research groups. Hence, the main goal of this thesis is to obtain the heat transfer coefficient on the endwall of a low-speed OGV linear cascade for CFD validation and produce data to compare it with previous experiments.

The results of the heat transfer for the different configuration of the endwall and vanes are discussed in this thesis.

Acknowledgement

First of all, I would like to express my gratitude to my supervisor Borja Rojo. This master's thesis never had been possible without his help. His patience for explaining and his hard work under pressure are worthy of admiration.

Thanks to Professor Valery Chernoray for giving me the opportunity of being part of the applied mechanics department.

I would also like to express my gratitude to Carlos Jimenez for teaching me everything that was required for the laboratory. His previous work in this field has been very useful in the project.

I am grateful to my mother, father and sister who are always there to support me, even in the toughest moments and because thanks to them i have become in the person who i am nowadays.

Lastly, to all my Erasmus friends who have been looking after me as a family this year. Mainly, Ana for tempering me when it was needed, and Isak for giving me a reason to look forward to coming to work everyday.

Contents

Abstract

1	Introduction and Objective	5
2	Theoretical Background	6
2.1	Heat Transfer	6
2.2	Conduction	7
2.3	Radiation	7
2.4	Convection	9
2.4.1	Turbulent flow over a heated flat plate	9
2.5	Theoretical Model	11
2.6	Guide for Experiments	13
2.7	Nondimensionalization	13
3	Experimental components and Measurements set up	15
3.1	The Endwall	15
3.1.1	Heat source	17
3.2	The vane and the window	18
3.3	Temperature sensors	19
3.3.1	Measurement and calibration procedure for RTD sensors	21
3.3.2	Uncertainty of measurements	22
3.3.3	Results of the calibration	24
3.3.4	Post processing to obtain the temperature map of the aluminium surface	28
3.4	IR Camera	30
3.4.1	IR camera set up	32
	Calibration devices	32
3.4.2	Image correction procedure	35
	1 Removal of Bad Pixels	35
	2 Removal of the Temporal Noise	37
	3 NUC	38

3.4.3	Calibration	43
3.4.4	Post processing to obtain the temperature map of the side wall	43
4	Heat transfer experiments	46
4.1	Jet impingement	46
4.1.1	Experimental set up	47
4.2	linear cascade	49
4.2.1	Flow measurements	52
5	Calculation of the Heat Flux in the Endwall	57
6	Results	59
6.1	Results for the jet impingement case	59
6.2	Results for the flat plate case	61
6.3	OGV cascade case	71
7	Conclusions	72
8	Future work	74
	Bibliography	78

Nomenclature

Abbreviations

CFD Computational fluid dynamics

EES Engine exit structure

HTC Heat transfer coefficient

OGV Outlet guide vane

Greek Symbols

α Absorptivity [-]

δ Boundary layer thickness [m]

λ Wavelength [μm]

μ Dynamic viscosity of fluid [$\frac{K}{s \cdot m}$]

ρ Reflectivity; fluid density [-][$\frac{K}{m^3}$]

σ Stefan Boltzmann constant [$\frac{W}{m^2 \cdot K^4}$]

τ Transmissivity [-]

ε Emissivity [-]

Subscripts

h Convection heat transfer coefficient [$\frac{W}{m^2 \cdot K}$]

k Thermal conductivity [$\frac{W}{mK}$]

k_{epoxy} Thermal conductivity of the epoxy [$\frac{W}{mK}$]

q''_{cd} Heat flux via conduction [$\frac{W}{m^2}$]

q''_{cv}	Heat flux via convection	$[\frac{W}{m^2}]$
q''_{rad}	Heat flux via conduction	$[\frac{W}{m^2}]$
Nu	Nusselt number	[-]
Pr	Prandtl number	[-]
Re	Reynolds number	[-]
v	Velocity of the air	$[\frac{m}{s}]$

Chapter 1

Introduction and Objective

The primary objective of the study is evaluate through empirical data and correlations the heat transfer coefficient on the endwall surface located in a low-speed OGV linear cascade. Knowing the heat transfer mechanisms involved can lead to predict accurately the maximum temperature or thermal load on the surface of this component, and therefore, estimate the cooling if needed or select a lighter material that can handle the predicted thermal loads without thermal damage.

The efficiency of propulsion jet engines could be increased by raising the temperatures in the combustor. This would mean that the temperature at the inlet to the engine exit structure (EES), where the OGVs are located, would be increased as well. Therefore, new materials or cooling systems would be required to stand the new thermal load on this structure.

The OGVs located in the EES are used for two structural purposes. First, this component connects the external casing and the core of the engine. In addition, OGVs provide access for oil tubes, oil-scavenge and electrical cables from the casing to the shaft. The aerodynamic function of the OGVs is to remove swirl from the flow after the low - pressure turbine.

This master thesis is a continuation of previous investigation in a low-speed large-scale linear cascade performed at Chalmers University of Technology. The main goals of this work are to obtain the convection heat transfer coefficient over the endwall surface in a low-speed linear cascade once its has been validated at different configurations of the endwall. The heat transfer that take place in the endwall is also studied. Our efforts have been focused as well in the image processing system coming from an IR camera used to measure temperature distributions over surfaces with the highest possible precision with our instruments, increasing therefore the accuracy of our results.

Chapter 2

Theoretical Background

To understand the phenomenas analysed in this work it is important to understand the heat transfer mechanisms. These are radiation, conduction and convection. The models explained below would be the base to validate the results of the experiments, concluding if the endwall and the method are trustworthy for the appraisal of the heat transfer.

2.1 Heat Transfer

A simple, yet general, definition of the heat transfer is: A thermal energy in transit due to a special temperature difference.

As shown in Figure 2.1, we refer to different types of heat transfer processes as modes. When a temperature gradient exists in a stationary medium, which may be a solid or a fluid, we use the term conduction to refer to the heat transfer that will occur across the medium. In contrast, the term convection refers to heat transfer that will occur between a surface and a moving fluid when they are at different temperatures. The third mode of heat transfer is termed thermal radiation. All surfaces of finite temperature emit energy in the form of electromagnetic waves. Hence, in the absence of an intervening medium, there is net heat transfer by radiation between two surfaces at different temperatures [11].

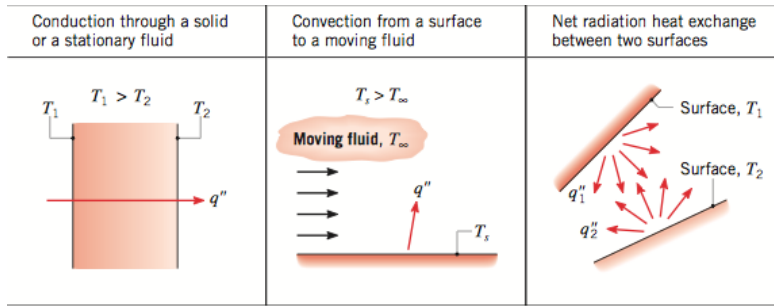


Figure 2.1: Conduction, convection, and radiation heat transfer modes [11]

2.2 Conduction

The conduction is the energy transfer from the most energetic particles to the less energetic particles of a substance due to interactions between the particles. Conduction is the type of heat transfer that takes place in the presence of a temperature gradient. Energy transfer via conduction must then occur in the direction of decreasing temperature. The law that mathematically shows this is **Fourier's Law**:

$$q''_{cd} = -k\nabla T \quad (2.1)$$

The heat flux $q''(\frac{W}{m^2})$ is the heat transfer conducted per unit area perpendicular to the direction of transfer, and it is proportional to the temperature gradient. The heat flux that is transported by conduction is also dependent on a material property known as thermal conductivity $k(\frac{W}{mK})$.

2.3 Radiation

Radiation is the emission or transmission of energy in the form of waves or particles through space or through a material medium.

Kirchoff's Law of Thermal Radiation This law yields that, at each wavelength absorption coefficient and emissivity have the same spectral value ($\alpha_\lambda = \varepsilon_\lambda$)

Black body A black body is an idealized physical body that absorbs all incident electromagnetic radiation, regardless of frequency or angle of incidence. A black body in thermal equilibrium (that is, at a constant temperature) emits electromagnetic radiation called black-body radiation. The radiation is emitted according to

Planck's law, meaning that it has a spectrum that is determined by the temperature itself, not by the body's shape or composition. A black body in thermal equilibrium has two notable properties:

1. It is an ideal emitter: at every frequency, it emits more energy than any other body at the same temperature.
2. It is a diffuse emitter: the energy is radiated isotropically, independent of direction.

By definition, a black body in thermal equilibrium has an emissivity of $\varepsilon = 1$.

All concepts about thermal radiation are developed from the Planck's distribution, which is shown below, that gives the spectral radiance of the black body, as a function of the wavelength and the temperature.

$$E_b(\lambda, T) \left(\frac{W}{m^3} \right) = \frac{C_1}{\lambda^5 (e^{\frac{C_2}{\lambda T}} - 1)} \quad (2.2)$$

$$C_1 = 3.742 \cdot 10^{-16} W m^2$$

$$C_2 = 1.4385 \cdot 10^{-2} mK$$

If we try to find where the maximum values of energy emitted occur we will find the wavelengths at which maximum values of E_b take place. These values follow the *Wien's Law*:

$$\lambda_{max} T = C_3 \quad (2.3)$$

$$C_3 = 0.002898 mK$$

Performing integration of the Planck Distribution over all the wavelength interval we can obtain the total emitted power of a Black Body only as a function of temperature and the *Boltzmann's Constant* ($\sigma = 5.67 \cdot 10^{-8} \frac{W}{m^2 K^4}$).

Thermal radiation is affected by the following properties: *reflectivity* (ρ), *absorptivity* (α) and *transmissivity* (τ). Absorptivity gives the portion of incident radiation that is absorbed by the body. Transmissivity gives the portion of radiation that is transmitted by the surface, and reflectivity is the portion of incident radiation that is reflected by the surface. According to these definitions and making a simple radiation balance, the expression (2.4) should be satisfied:

$$\alpha + \tau + \rho = 1 \quad (2.4)$$

Also is required to take into account the concept of the energy coming into a surface which is emitting energy with a certain emissivity and absorbing it with a certain absorptivity represented by G .

Combining the theory which involves these characteristics the net rate of radiation heat transfer from the surface, expressed per unit area of the surface, is:

$$q''_{rad} = \varepsilon\sigma(T_s^4 - T_{sur}^4) \quad (2.5)$$

Where T_s is the temperature of the surface and a much larger, isothermal surface that completely surrounds the smaller one (T_{sur}). This expression provides the difference between thermal energy that is released due to radiation emission and that gained due to radiation absorption. The highest emissivity reachable is the one given by a black body.

The radiation has a crucial role in this project. The temperature of the surface exposed to the air flow is going to be measured with an IR-camera. This is the reason for applying a special coating in order to achieve an emissivity factor of 0.973 (almost black body), constant for our range of study.

2.4 Convection

The convection heat transfer mode can be described as energy transfer occurring within a fluid due to the combined effects of conduction and bulk fluid motion. Typically, the energy that is being transferred is the sensible, or internal thermal, energy of the fluid. Convection is dependent of many variables such velocity, density, dynamic viscosity and fluid temperature as it has a very big relation with the fluid flow. In our experiments we are interested in measuring the heat transfer between a surface and the fluid surrounding it. To approach a quantitative analysis of convection, *Newton's Law* is used:

$$q''_{cv} = h(T_{surface} - T_{\infty}) \quad (2.6)$$

Where $q''_{cv}(\frac{W}{m^2})$ is the convective heat flux, proportional to the temperature difference between the surface and fluid, T_s and T_{∞} respectively. The parameter $h(\frac{W}{m^2K})$ is termed the convection heat transfer coefficient. This coefficient depends on conditions in the boundary layer, which are influenced by surface geometry, the nature of the fluid motion, and an assortment of fluid thermodynamic and transport properties. It is important to note that T_{∞} is the temperature of the fluid far away enough from the surface so that the temperature distribution can be considered constant (far from the thermal boundary layer).

2.4.1 Turbulent flow over a heated flat plate

The experimetns covered by this Master thesis are an especial case of external flow. For the calculation of the Nusselt number in our experiments (except from

the impinging jet) an unheated starting length ($T_s = T_\infty$) upstream of a heated section ($T_s \neq T_\infty$). In a case of external flow over a flat plate the velocity boundary layer development begins at $x=0$, while in our case the thermal boundary layer development begins at $x = \xi$. Hence there is not heat transfer for $0 \leq x \leq \xi$. Through use of an integral boundary layer solution, it is known that, for turbulent flow, the *Nusselt* number is:

$$Nu_x = \frac{Nu_x |_{\xi=0}}{[1 - (\xi/x)^{9/10}]^{1/9}} \quad (2.7)$$

The characteristic length x is measured from the leading edge of the unheated starting length. As it could be seen in Figure 2.2.

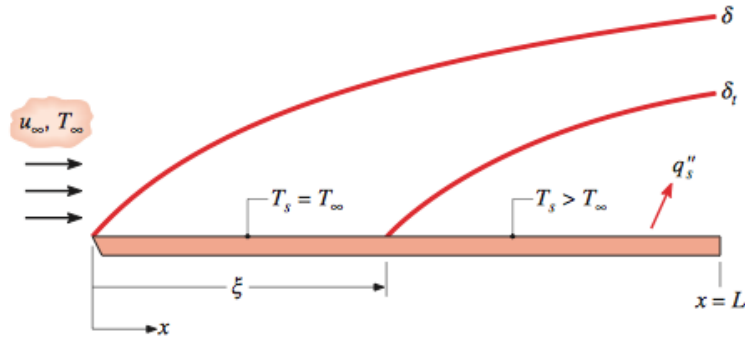


Figure 2.2: Flat plate in parallel flow with unheated starting length [11]

Two assumptions could be done for the equation above to determine the *Nusselt* number for a turbulent flow:

1. Constant temperature.

Where the Nu_x number is given as:

$$Nu_x = StRe_x Pr = 0.0296 Re_x^{4/5} Pr^{1/3} \quad 0.6 < Pr < 60 \quad (2.8)$$

2. Constant heat flux.

Where the Nu_x number is given as:

$$Nu_x = 0.0308 Re_x^{4/5} Pr^{1/3} \quad 0.6 < Pr < 60 \quad (2.9)$$

In the case of the experiments Pr is going to be simplified as constant since in the interval of 22°C to 32°C the error is about 0.1% on the Pr . The used value for Pr is 0.71 .

Boundary Layer The boundary layer is the zone where the velocity of the fluid is between zero and 99% of the free-stream velocity. This area near wall inside the flow field is dominated by the viscous forces.

The viscous nature of airflow reduces the local velocities on a surface and is responsible for skin friction. The layer of air over the wing's surface that is slowed down or stopped by viscosity, is the boundary layer. There are two different types of boundary layer flow: laminar and turbulent.

At some distance from the leading edge, the smooth laminar flow breaks down and transitions to a turbulent flow.

The boundary layer is considered as all the resistance of the heat transfer, defined as:

$$q = kA \frac{T_{wall} - T_{fluid}}{\delta} \quad (2.10)$$

This equation is a simplification, more details can be founded in [2]. For turbulent flow, boundary layer development is influenced strongly by random fluctuations in the fluid and not by molecular diffusion. For the previous calculations defined in the range of the values of the linear cascade cases, the following equation is used:

$$\delta = 0.37 Re_x^{-1/5} \quad (2.11)$$

2.5 Theoretical Model

To sum up, energy conservation is applied at the surface of the body. The heat transfer obeys the **Law of conservation of energy** and if the conditions are steady, the energy balance is shown in equation 2.12 and Figure 2.3 shows the theoretical model used in all the experiments.

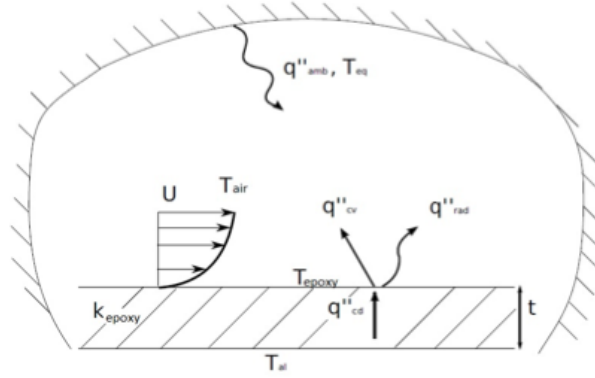


Figure 2.3: Theoretical model for the *HTC* experiment

$$q''_{cond} = q''_{conv} + q''_{rad} \quad (2.12)$$

We can express each of the terms using the appropriate rate equations. In the case of the experiments developed for this master thesis the heat fluxes are calculated as:

1. Conduction heat flux:

$$q''_{cd} \simeq k \frac{T_{aluminium} - T_{epoxy}}{t} \quad (2.13)$$

2. Radiation heat flux:

$$q''_{rad} \simeq \varepsilon \alpha (T_{epoxy}^4 - T_{amb}^4) \quad (2.14)$$

3. Convection heat flux:

$$q''_{cv} = h(T_{epoxy} - T_{airflow}) \quad (2.15)$$

Our experimental model is made of a thick aluminium core covered by a layer of epoxy. And it is measured the temperature of the core and the surface. The gradient of temperature of interest to obtain the heat flux via conduction is between the air-epoxy interface and the aluminium-epoxy interface. This fact is explained in detail in section 3.1 . The parameter T_{amb} is the room temperature.

To calculate the parameter h called *HTC* in the rest of the report, the thermal emissivity of the black coating is specified as = 0.973 (section 3.2). The *HTC*

equation for this project, after the data reduction and the assumptions required for the model, is defined as:

$$HTC = \frac{k \frac{(T_{aluminium} - T_{epoxy})}{t} - \varepsilon \alpha (T_{epoxy}^4 - T_{amb}^4)}{T_{epoxy} - T_{airflow}} \quad (2.16)$$

This equation is an 1D approach for solving the heat transfer coefficient problem.

2.6 Guide for Experiments

This is a listing requirement for initiating and executing a successful aerodynamic experiment adapted from [1].

1. The propose of the experiment is to obtain the convection heat transfer coefficient over the endwall and OGV placed in a linear cascade. The results from the experiments carried out will have associated expected accuracy and precision. The accuracy and precision requirements will be part of the problem statement.
2. Identify the outcomes needed, including the ranges of the values of parameters that will provide the information to resolve the problem. There will be required accuracies and precisions associated with each variable or parameter that should be identified.
3. Identify feasible model provisions and compatible facilities. This will require conceptual and preliminary design of the models and fixtures.
4. Prove the trustworthy of the results and the design comparing with the sources required.
5. Initiate the experiment. Provide equipment for monitoring of all the processes and data gathering. Include process evaluation of achieved accuracies and precision in measurements.
6. Conduct data analyses to provide quantitative evaluation of the achieved accuracies and precisions.

2.7 Nondimensionalization

To identify the outcomes needed, as the guide for the experiments points, a very useful technique to clarify the parameters to consider is applied, nondimensionalization.

Nondimensionalization is the partial or full removal of units from an equation involving physical quantities by a suitable substitution of variables. This technique can simplify and parameterize problems where measured units are involved. It is closely related to dimensional analysis. For the experiments carried out during this project, the ultimate goal is to achieve the $HTC(\frac{W}{m^2K})$, although it is a very complex value to obtain this value analytically as it is dependent on the fluid flow and certain properties of the surface. However, with the theoretical model we are going to assume that the necessary parameters for the HTC are:

$$HTC = f(u, \rho, \mu, x, k, c_p) \tag{2.17}$$

Chapter 3

Experimental components and Measurements set up

3.1 The Endwall

The wall used in the heat transfer experiments is an improved version of another design by Carlos Jimenez [5]. The designed drawn by Saul Josep Llacer [6] was build by different workshops. The main requirement is that the temperature in the aluminium-epoxy interface could be measured with 21 Pt 100 and obtain a temperature distribution comparable to what Saul predicted numerically in his thesis. As it can be seen in the set up of the experiments in Chapter 4 the surface in contact with the air should have the highest emissivity as possible. This is the reason why this surface is coated as it is explained in section 3.4. The thermal conductivity of the material in contact with the air must be low in order to obtain a significant thermal gradient (for our temperature sensors) between the aluminium-epoxy interface and the epoxy surface. This is the reason to choose epoxy for this purpose. In the previous version of the wall this layer was made of plexiglass, material which gave problems in the experiments and not enough accurate results. It was clearly specified to the epoxy workshop, how important was to achieve the highest flatness on the epoxy after milling process and the importance of avoid air bubbles which would interfere in the heat transfer.

The other surface is heated so that the aluminium material was selected taking into account that it should be good conductor and not deformable by heat. The sensors used to measure the temperature in 21 points of this surface were glued to prevent air gaps hampering in the results.

The aluminium surface was covered with a thick layer of insulating material to

minimize the heat losses. The holes made in the insulation material for the cables were joint with an liquid elastic material in order to minimize the losses as well. The finished endwall after entering the temperature sensors and connecting the heaters is shown in Fig. 3.1:

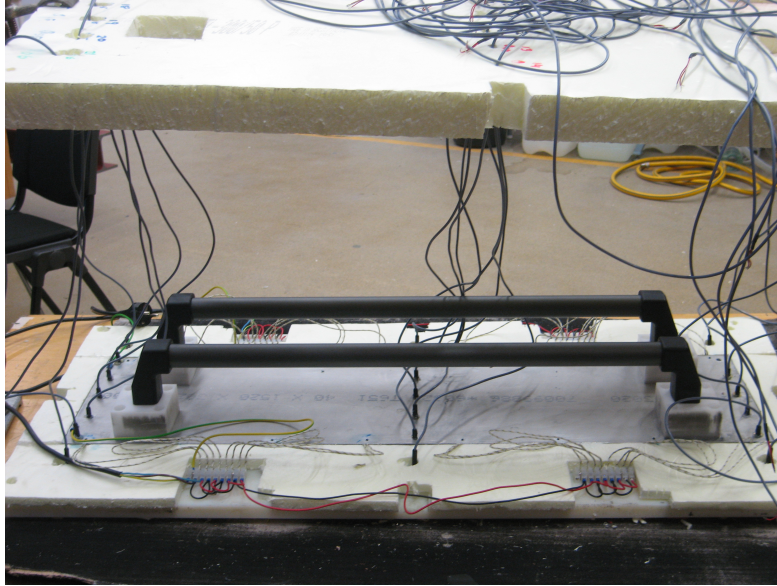


Figure 3.1: Endwall

As it was predicted in [6], the temperature of the temperature sensors of the corners was 3°C less than the others (Fig.3.2), but this difference is not so pronounced when the fan of the linear cascade in the second heat transfer experiment is switched on.

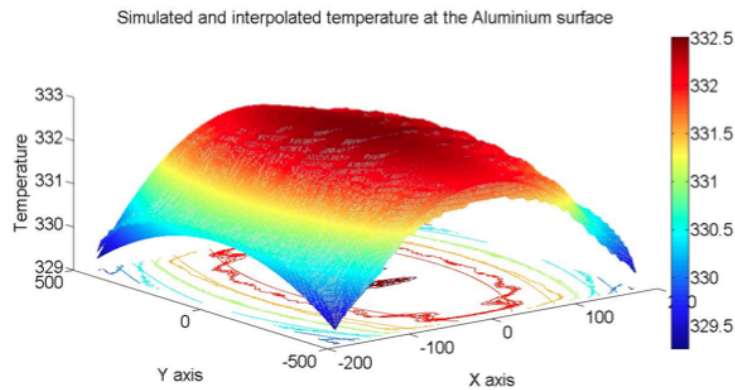


Figure 3.2: Temperature distribution from finite elements analysis (FEA) in Soliworks at the aluminum-epoxy interface

3.1.1 Heat source

Different configurations with a variable number of heaters were studied before the tests. Between the cases of heating the wall with 16, 24 or 30 heaters, the option with 16 heaters is selected since the error given by this distribution is lower than 0.1°C [6]. This value is desired as the maximum error in the temperature measured after the calibration of the Pt 100.

The heater characteristics are: 10mm x 100mm, 120V, 400W. 16 heaters are inserted in the aluminium core as a heat source, 8 per each side in groups of four as shown in Fig. 3.3. The resistance of the 8 heaters in parallel is 14 ohms. For the jet experiment, a current source of 4.5 [A] in total was used, while for the flat plate and OGV cascade more power was required to heat the flat plate so that two current sources were connected. The area of the cables were calculated with a high safe margin in order to stand that power. In addition, to make the experiments safer, a ground connection is installed to prevent a short circuit. In order to avoid any risk the last check was done with a multimeter. The connection is shown in the following figures:

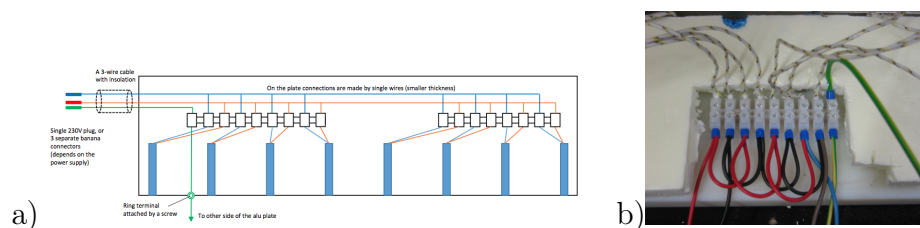


Figure 3.3: a) Wiring diagram b) Connection of four heaters

3.2 The vane and the window

Once the wall is ready and placed in the linear cascade, a plexiglass panel is placed in front of the wall to enclose the flow. But this pose a problem for taking the pictures since the IR-camera is not able to capture the area of interest through this kind of material. Due to the fact that the IR camera can only capture thermal radiation for the interval of $3 - 5\mu m$ of wavelength, two windows were machined on the plexiglass [5]. Two hinges with springs actuators take the role of the opening the small windows. The opening time in order not to affect the characteristics of the flow should be the minimal as possible. The error introduced by the time and the opening window is $0.15^\circ C$. This error is checked with the images post process. Figure 3.5 is the overview of the assembling of the endwall with the window and the mounted vanes designed by Carlos Sanchez.

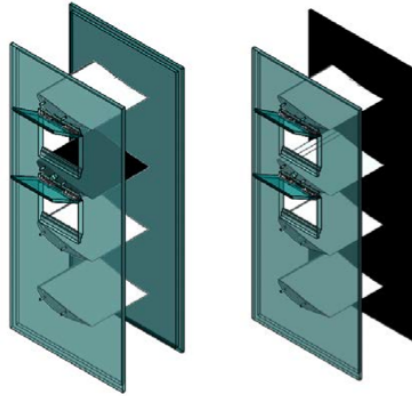


Figure 3.4: Overview of the assembling of the endwall the vanes and the window

The design of the vanes used in the experiment was provided by GKN. Three out of four vanes are manufactured using stereolithography process and a fourth one was manufactured with an aluminium core and 3mm shell for the same purposes as the endwall. The last vane was covered with silicon avoiding the air bubbles, coated as the endwall and marked with a three axis linear traversing system using a marker which thermal emissivity is lower than the coating and the points created can observed during the post processing of the images.



Figure 3.5: Acrylic sidewall with mounted vanes for the OGV cascade case experiment

3.3 Temperature sensors

The temperature sensor used in the project to measure the aluminium surface is a Pt 100 bought from RS Components. The size of the sensors is defined by its diameter ($\phi 6mm$), which is the necessary size to be fixed into the holes located in the aluminium plate of the endwall; more information about the data sheet can be found in the appendix 8.

The measure of the sensor's resistance at different temperatures can be converted in a temperature through a table which has been standardized by DIN, shown in Fig. 3.6. The correlation between resistance and temperature is based in the following equations:

For the range $-20C$ to $0C$ the interpolation equation is:

$$R(T) = R_0(1 + AT + BT^2 + Ct^3(T - 100)) \quad (3.1)$$

But in the experiment the interval of temperatures is going to be between $0C$ and $60C$, so the interpolation equation is:

$$R(T) = R_0(1 + AT + BT^2) \quad (3.2)$$

Equations 3.1 and 3.2 are known as Callendar-Van Dusen equations. Coefficients A, B and the temperature tolerances are estimated from experimental results.

$$A = 3.9083 \cdot 10^{-3}(C)$$

$$B = -5.775 \cdot 10^{-7}(C^2)$$

$$\text{Class A tolerance} : \pm(0.15 + 0.002 \cdot T)$$

In the experiment, the accuracy of these sensors is crucial therefore a calibration was carried out to improve the measurement accuracy. The equipment, method and results are explained below.

RESISTENCIA NOMINAL: 100 OHMS A 0°C

°C	0	-10	-20	-30	-40	-50	-60	-70	-80	-90	-100
-200	18.44	14.26	10.35	7.06	4.49	2.52	—	—	—	—	—
-100	60.20	56.13	52.04	47.93	43.80	39.65	35.48	31.28	27.03	22.71	18.44
0	100.00	96.07	92.13	88.17	84.21	80.25	76.28	72.29	68.28	64.25	60.20

°C	0	1	2	3	4	5	6	7	8	9	10
0	100.00	100.39	100.78	101.17	101.56	101.95	102.34	102.73	103.12	103.51	103.90
10	103.90	104.29	104.68	105.07	105.46	105.85	106.24	106.63	107.02	107.40	107.79
20	107.79	108.18	108.57	108.96	109.35	109.73	110.12	110.51	110.90	111.28	111.67
30	111.67	112.06	112.45	112.83	113.22	113.61	113.99	114.38	114.77	115.15	115.54
40	115.54	115.93	116.31	116.70	117.08	117.47	117.85	118.24	118.62	119.01	119.40
50	119.40	119.78	120.16	120.55	120.93	121.32	121.70	122.09	122.47	122.86	123.24
60	123.24	123.62	124.01	124.39	124.77	125.16	125.54	125.92	126.31	126.69	127.07
70	127.07	127.45	127.84	128.22	128.60	128.98	129.37	129.75	130.13	130.51	130.89
80	130.89	131.27	131.66	132.04	132.42	132.80	133.18	133.56	133.94	134.32	134.70
90	134.70	135.08	135.46	135.84	136.22	136.60	136.98	137.36	137.74	138.12	138.50
100	138.50	138.88	139.26	139.64	140.02	140.40	140.77	141.15	141.53	141.91	142.29
110	142.29	142.66	143.04	143.42	143.80	144.18	144.55	144.93	145.31	145.68	146.06
120	146.06	146.44	146.82	147.19	147.57	147.94	148.32	148.70	149.07	149.45	149.82

Figure 3.6: RTD Pt 100 conversion Table

3.3.1 Measurement and calibration procedure for RTD sensors

The measurement flow for RTD sensors is illustrated in the following map diagram.



Figure 3.7: Map diagram of the measurement and process of the data

The first circuit represents the link between each three wire RTD (Pt 100) with the internal circuit of the USB NI 9217 Measurement System. NI 9217 is a module which can provide 1 mA of current excitation per channel and has less than a 1 °C accuracy error over its entire operating temperature range. The NI 9217 has NIST-traceable calibration and includes a channel-to-earth ground double isolation barrier for safety and noise immunity. NI CompactDAQ is the platform device, six modules can be working simultaneously, and per each module four Pt 100 can be coupled, so six modules were required to operate the twenty-one Pt 100 used in the experiments.



Figure 3.8: NI CompactDAQ

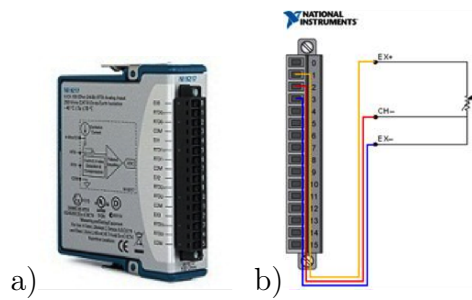


Figure 3.9: a) NI 9217 module b) Connexion with the Pt 100

Following the Map diagram, LabView is the software which was used to analyze, present, and manage the data. This program gives the possibility of programming a control panel to show by graphing changes in temperature on time. The third step is export the measurements to an excel file. Afterwards these data is processed in Matlab.

To run the LabView program, two inputs are required to define the sample rate: Hz and number of samples. The ratio of these parameters determines the sampling time. In this case, in order to obtain the best accuracy possible, 0.2 s sampling time was selected. These is equivalent to 50 frequency and 10 samples. In the uper left corner shown in Fig. 3.10 the number of samples can be seen.

The heat source is a temperature controlled water bath, this device has a variation of 1°C between the temperature introduced like input and the real one measured by the mercury thermometer. It could be seen in the Figure 3.14. The temperatures of the water to calibrate the RTD were 0°C, 25°C , 50°C, 60°C, 70°C, 80°C, 90°C and 100°C. The expectations of the veracity were higher in 0°C and 100°C points to be critical points in the water diagram. To be more exact, 100.2°C is the boiling point at 1.02 bar, ambient pressure at the laboratory. The measurements of 0°C and 50°C were redone in different days to check that environmental conditions were not a variable to consider. The RTD was covered with film paper to protect the plastic of the sensor since its melting point is at 170°C.

3.3.2 Uncertainty of measurements

Typically the temperature in the bath was stabilized after less than 1800 s. When the steady conditions were reached, the data samples were taken, a graphic temperature-time and a histogram was and analyzed in Matlab for each temperature setpoint, as shown in Fig. 3.11.

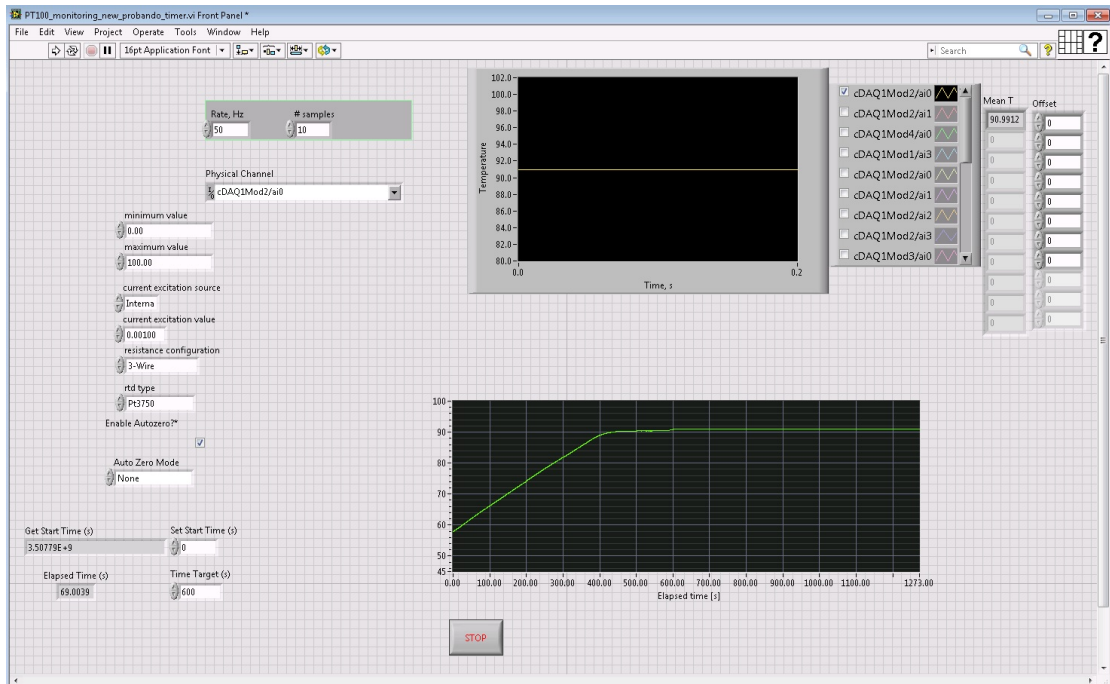


Figure 3.10: LabView front panel and diagrams

This temperature distribution is a sinusoidal due to the PI integrated in the temperature bath. The variation between the maximum and minimum value is 0.01°C therefore it can be assumed constant. Figure 3.11 b) shows a histogram of 3003 samples. The distribution appears within the bounds that can be considered normal, although no consistency checks have been conducted. It is assumed that the samples at each temperature are normally distributed. This fact is represented by the red line in Fig. 3.11, calculated with a mean of 25.68°C and a standard deviation of $7.4^{-04^{\circ}\text{C}}$. From now, instead of the the row data obtained in each experiment, this data will be reduced to the mean value for post processing purposes.

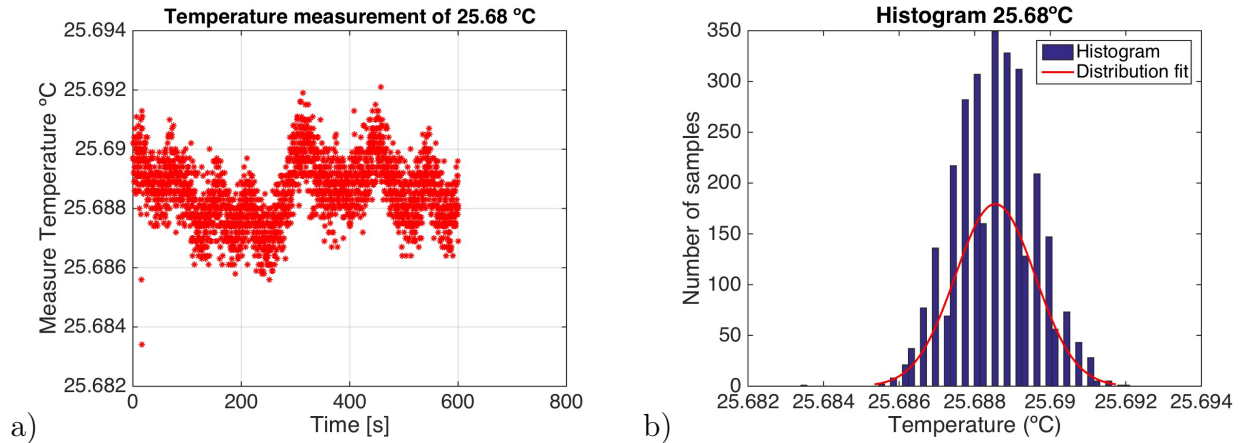


Figure 3.11: a) Temperature raw data b) Temperature histogram

The other source of error which must be taken into account is the resolution of the mercury thermometer (0.1°C), which is represented in Fig. 3.12 and 3.13 by the red whisker plot.

3.3.3 Results of the calibration

The goal of the calibration is to reach a linear relationship between the actual temperature, measured by the mercury thermometer, and the temperature measured with the Pt 100. The last square method was used to obtain the linear fit coefficients. The final equation would be:

$$y = a \cdot x + b$$

where a and b are constants.

$$a = \frac{(n \cdot \sum xy) - (\sum x \sum y)}{(n \cdot \sum x^2) - (\sum x)^2} \quad b = \frac{(\sum y) - (a \cdot \sum x)}{n}$$

The meaning of the variables is explained in Table 3.1. Through this section will be proved how necessary is the calibration of the Pt 100 since even adding the temperature tolerance given from the product manufacturer, the temperatures measured with the Pt 100 differs up to 0.2°C from the temperature measured by the mercury thermometer.

A non linear response at high temperatures was expected, which is visible in Fig.?? from 70°C and above. Temperatures above 70°C will not be reached during the experiments. Therefore, in order to improve the accuracy of the Pt 100 measurements the least line square is calculated for temperatures below 65°C .

Variable	Definition
X	Temperature measured by the Pt 100
Y	Actual Temperature
n	Number of matching XY data pairs
a	Slope or tangent of the angle of the regression line
b	Y-Intercept (y value at x=0)
Σx	Sum of all X data values
Σy	Sum of all Y data values
Σxy	Sum of products of all matching XY data pairs
Σx^2	Sum of squares of all X data values

Table 3.1:

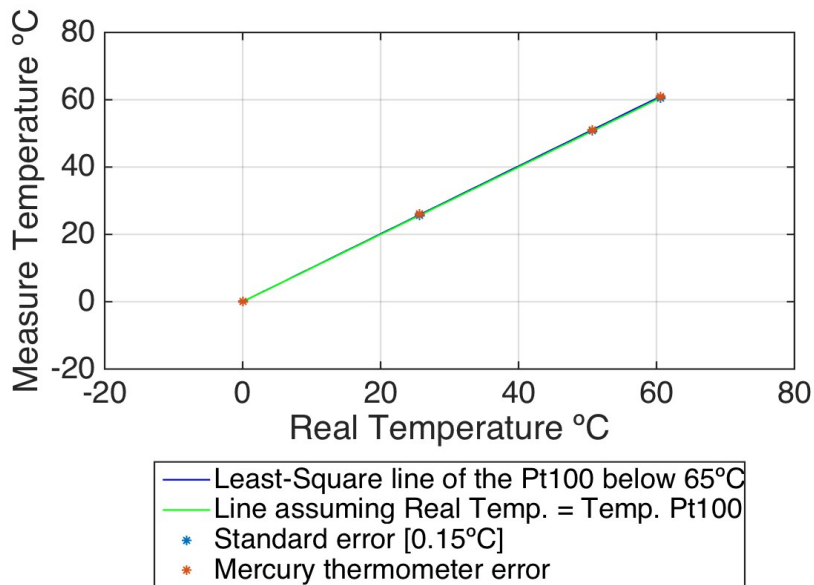


Figure 3.12: Least square line fit for temperatures

A zoom in over the area of the whiskers plots provide the proof of the importance of the calibration. If the mercury thermometer temperature is considered as the real one, it is shown how the temperature measured with the Pt 100 is displaced enough to be out of range, even if the 0.15°C are added (green line of the figure). The range considered for the calibration is the temperature measured with the mercury thermometer $\pm 0.15^{\circ}\text{C}$. On the other hand, it is discernible how the least square line calculated with the mean of the temperatures below 65°C is

within the desired limits.

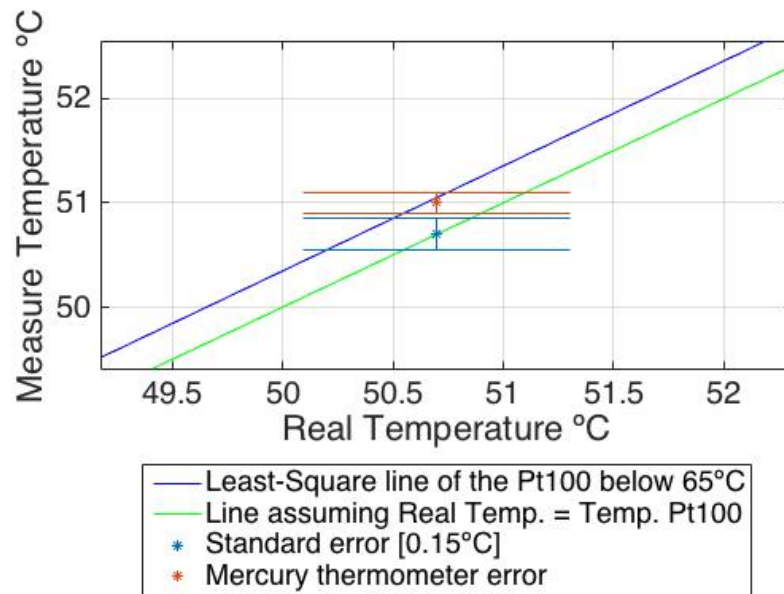


Figure 3.13: Zoom of the Least square line fit temperatures

A validation is required to complete the calibration. It was based on the comparison of the least square line achieved and the standard graph by DIN.

This project uses 21 Pt 100 to measure the temperature along the aluminium surface. The same process was done connecting all the Pt 100 at the same time. Twenty channels were included in the LabView program and the Matlab code was developed to process the new matrix of data. Figure 3.14 shows the calibration in the PI system.



Figure 3.14: 21 Pt 100 in the calibration bath

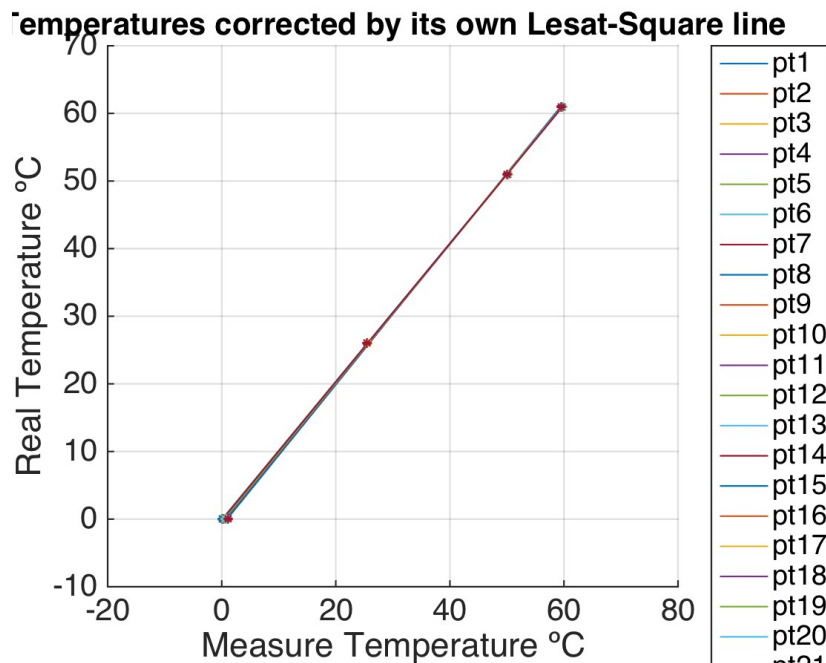


Figure 3.15: Calibration lines for the 21 Pt 100

Figure 3.15 shows the calibration for all the sensors.

3.3.4 Post processing to obtain the temperature map of the aluminium surface

The twenty-one Pt 100 in the experiment give the temperature of twenty-one points of the aluminium surface, nevertheless the aim of the experiments it is not to calculate the heat transfer coefficient at few locations. The goal is to measure the heat transfer coefficient among the entire surface with high resolution. It is not possible to assume that the heat and temperature are uniformly distributed. Therefore, four types of interpolations are calculated with Matlab in order to achieve a temperature distribution: *Linear*, X^2Y^2 , *Cubic* and *V4*. The most appropriate interpolation is saved as the mapping temperature of the aluminium surface. This will be an input that would be required for the last post processing program to calculate the heat flux and therefore, the heat transfer coefficient.

The inputs for the Matlab script are the twenty-one temperatures measured with the sensors and the coordinates (x,y) to locate them in a grid which represents the endwall as it could be seen in Fig.3.16 with the black dots. The distributions are shown in Fig.3.17. The main characteristics of the different interpolation methods are:

- *Linear*: Triangulation-based linear interpolation.
- X^2Y^2 : Interpolation based on polynomial of X^2 , Y^2 and possible combination between these terms and lower terms [6].
- *Cubic*: Triangulation based cubic interpolation method.
- *V4*: Biharmonic spline interpolation. Unlike the other methods, this interpolation is not based on a triangulation. It is a radial basis function.

Figure 3.17 is an example of the aluminium distributions in the jet experiment. As it could be see in Fig. 3.17 d) the v4 interpolation allows identify where exactly the jet is located. Nevertheless, the interpolation is not as accurate as the others one for the whole surface.

For all the cases the polynomial proposed by Saul [6] has been chosen since it is representative of what can be expected inside the aluminum core.

The X^2Y^2 interpolation of the aluminium surface is stored as a .txt file to be used by Matlab and in a .prof file as a Fluent input for the calculation of the convection heat transfer coefficient.

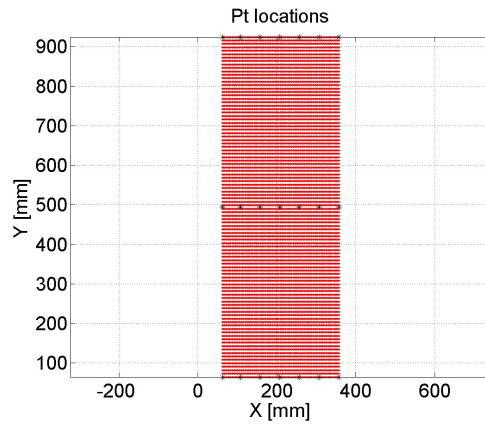


Figure 3.16: Grid required for the interpolation of the temperature on the aluminium surface with the location of the Pt 100

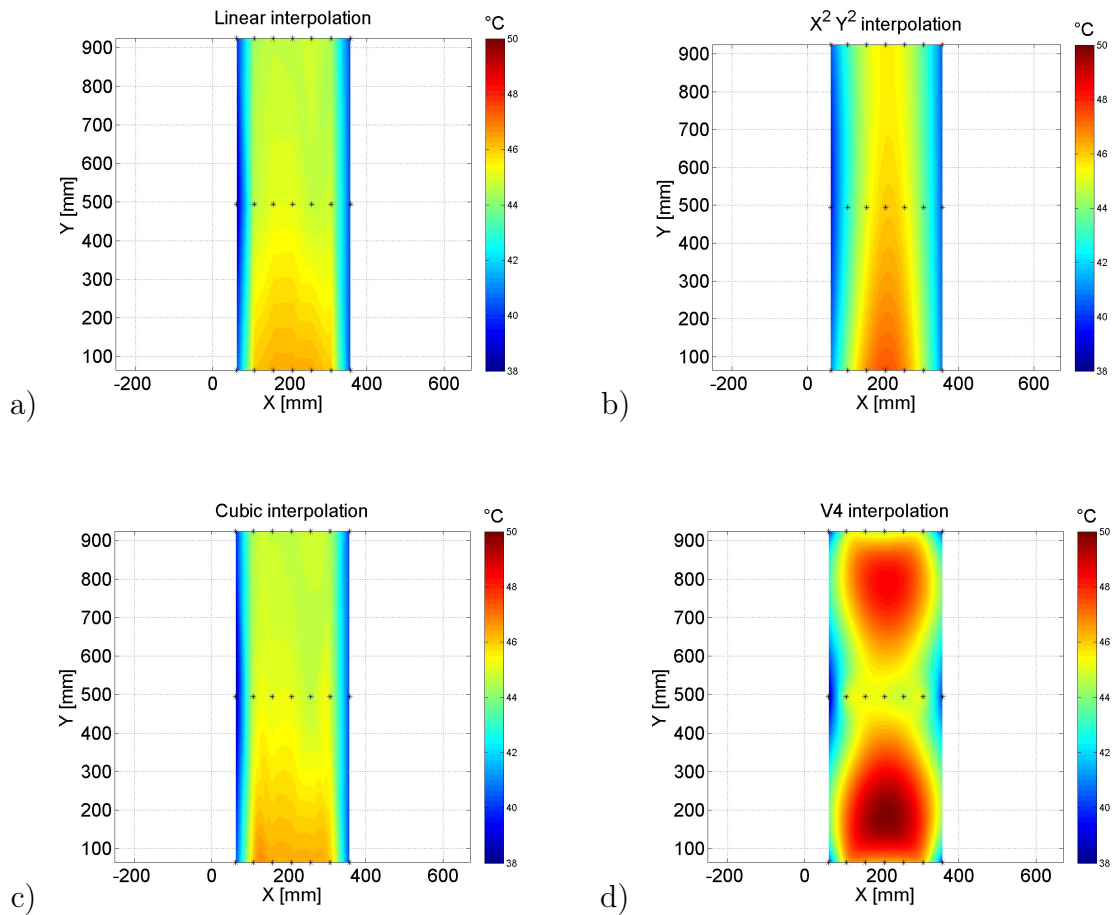


Figure 3.17: a) Linear interpolation b) Polynomial X^2Y^2 interpolation c) Cubic interpolation d) V4 Greens' function approach interpolation

3.4 IR Camera

The temperature measurements of the epoxy surface are made with a IR-camera. The IR camera is a MWIR Phoenix Camera System with a 320x256 resolution. There are two lenses for the camera, one would be used for the Jet test and another with wider view angle for the flat plate and OGV cascade experiments. Table 3.18 shows the camera specifications.

<i>Manufacturer</i>	Flir Systems Inc.
<i>Model</i>	Phoenix MWIR Camera System
<i>Detector type</i>	Indium Antimonide
<i>Detector spectral response</i>	1 μm - 5.4 μm
<i>Filtered spectral response</i>	3 μm - 5 μm
<i>Format (pixel number, HxV)</i>	320 x 256
<i>Detector pitch</i>	30 μm
<i>Detector cooling</i>	Stirling cycle
<i>Detector temperature</i>	77 K
<i>Dynamic range</i>	14 bit
<i>Noise equivalent temperature difference (sensitivity)</i>	25 mK
<i>Minimum window</i>	2 rows x 4 columns
<i>Integration mode</i>	Snapshot
<i>Max frame rate full window</i>	122 Hz.
<i>Max frame rate minimum window</i>	13.6 kHz
<i>Integration time</i>	9 μs - 16.6 ms
<i>Output</i>	Composite video / digital image / RS.232 camera control
<i>Input</i>	Sync (arm/trigger) / RS 232 camera control
<i>Optics</i>	25 mm f/2.3 MWIR / Janos Technology

Figure 3.18: Camera specifications

In order to reduce the effects of the environment on the measurements of the temperature and heat transfer coefficient, the best practice is to use a test body with highest emissivity (and hence, absorptivity) as possible. This is the reason why a painting treatment for the endwall is necessary, to obtain the highest emissivity possible.

The paint used is the Nextel Vetel-Coating 811-21 from Mankiewicz Gebr. & Co. This paint has to be diluted in Nextel thinner 8061. The mix has to be liquid enough since the coating will be applied with a spray gun. It is made of 70% paint and 30% thinner which is filtered with a grill to remove any lumps. Table 3.2 shows the specifications of this coating.

During the painting treatment several layers of paint are applied on the targets. It is required to wait a few minutes until the paint is dry to apply an other layer.

Property	Value	Comments
ε (emissivity)	0.973	Constant for our work range
Maximum angle for constant ε	30°	60° for 1 percent drop
Thermal Conductivity	0.2 $\frac{W}{mK}$	Constant for our work range

Table 3.2: Black coating properties

More information about the coating procedure can be found in appendix 8. After the treatment result is a black surface with a smooth matte finish.

3.4.1 IR camera set up

In order to maximize the temperature precision, the first step is to choose the integration time and to select the non-imaging mode. The variation of this parameter moves the distribution of counts that the detector measures closer or further from the saturation point of the camera (16384 counts).

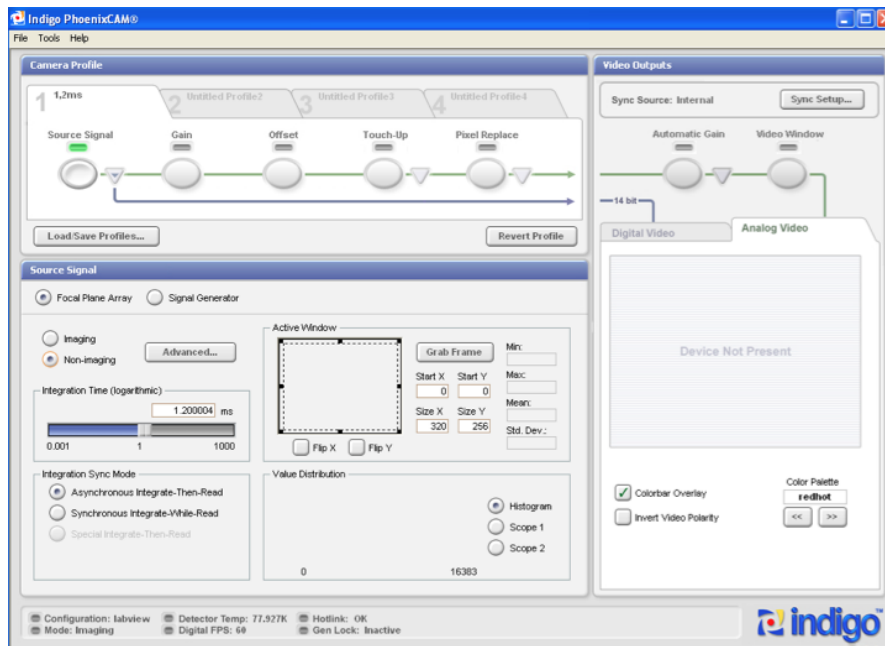


Figure 3.19: Camera software

The suitable integration time is the number which links the highest temperature that we want to measure, adding 5°C as a safety margin, with the maximum level of counts allowable with the camera (around 90 % from the saturation point). The interval of temperatures in the experiment is from 25°C to 55°C and it must be taken into account for adjusting this input. Furthermore in order to maximize the measurement accuracy of the camera, the camera must be calibrated.

Calibration devices

As calibration device and study rig for the transparent IR window two black bodies have been used. One of them is for the room temperature which would be the cold source needed for the NUC (section 3.4.2) and it is shown in Fig. 3.22. The other one is used to measure inside the mentioned interval of temperatures which are also needed for the NUC. The device shown in Figure 3.21 is capable to maintain the temperature from 25°C to 100°C by a water bath with a PI temper-

ature control. It uses heated water circulation through an aluminium box. The surface is coated with the same black paint as for the endwall.

The aluminium box is covered by insulation material to avoid heat losses, leaving free a circular hole, placed in the middle of the device. This region will be pointed at the camera to get the surfaces with uniform temperature distribution. In addition the uniformity of the temperature in the calibration surface is really important when performing calibration and correcting the images from the camera.

The black surface was placed horizontally above the IR-camera with the apparatus looking up in order to reduce temperature differences on the surface due to natural convection.

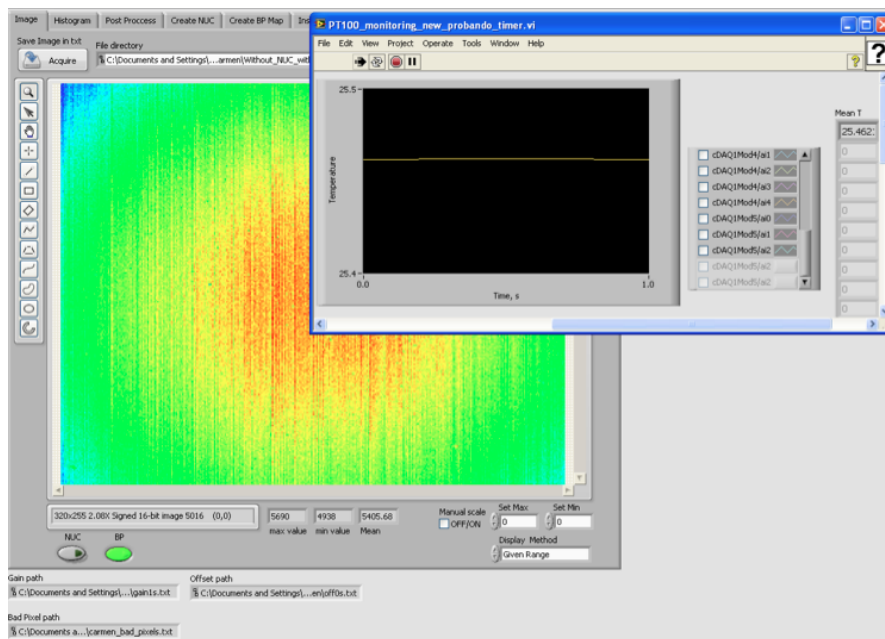


Figure 3.20: LabView programs

The reference temperature inside the box is measured with a Pt 100. Figure 3.20 shows the calibration software used. Two different LabView programs were used simultaneously for this purpose.

The surface of both bodies has to be treated to maximize its emissivity so that we do not get reflections because they would influence the data acquired by the IR-camera and, therefore, decrease the precision or add an unknown source of error.

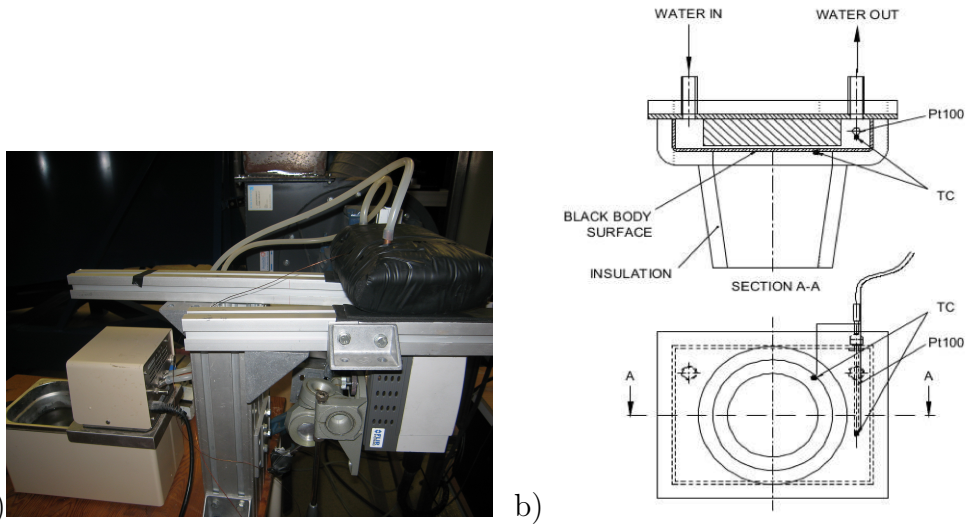


Figure 3.21: a) Black surfaces at different temperatures used for the calibration of the IR-camera [2] b) Drawing of the black body with a section view [2]



Figure 3.22: Cold source used for the calibration of the IR-camera

3.4.2 Image correction procedure

The core operating detector device, imaging systems with infra-red sensors, or as the acronym suggests IRFPA (Infrared Focal Plane Array), introduces a deterioration in the output of considerable magnitude depending on the purpose for which the images are captured. The deterioration factors are inherent to the detector mechanism, they are electronic and thermal noise. This noise is produced in the semiconductor devices due to load flow and interaction between them, commonly called temporal noise. In addition, the IRFPA are arrays of infrared radiation detectors, for example in our case 320x256. Different gain and offset parameters include in the model of the detector are generated between each of these pixels with its neighbors. Due to the non calibration, a pattern noise can be identified called by researchers as Spatial Noise or "non-uniformity" [3].

The conjunction of the effects mentioned above cause a deterioration in the output image which can reach such extreme levels that is likely to be unintelligible to the human eye. Hence, to solve this problem, the non-uniformity correction (NUC) is performed.

In this subsection the corrections and improvements made during this work period on the camera setup are presented.

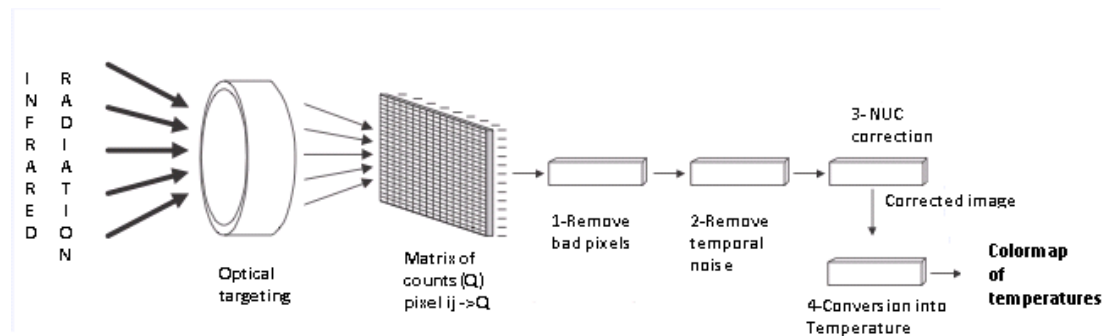


Figure 3.23: Process correction for the images and transformation in temperatures

1 Removal of Bad Pixels

The levels measured by the individual pixels should all be close to the average level measured. In case the level measured by a pixel diverge excessively from the average level, or if a high noise level is present, the pixel is labeled as a bad pixel. Pixels that cannot be corrected by a NUC procedure are also labeled as bad pixels. Bad pixels have to be corrected because they have a large impact on the quality of both the image quality and the accuracy of the measured data. [4]

In practice, a few bad pixels are going to be detected since they are going to measure out of the range. The range is the confidence interval calculated applying statistical analysis. This interval is calculated with the mean of the pixels and the standard deviation, assuming that the histogram of the values adjusts to a normal distribution.

This is something that has to be corrected along with the NUC in order to obtain a good post-processed thermal image. With this analysis, the location of the pixels that are out of our confidence interval will be seen as Fig. 3.24 shows. What follows is a lineal interpolation for these pixels with their surrounding ones, improving the accuracy of the scale. There is only one condition for this algorithm to be effective, namely that the neighboring pixels should not be a bad pixel. The bad-pixel replacement process is performed by the camera in real-time.

In the following figures illustrate the bad pixel locations and an image before and after the BP correction :

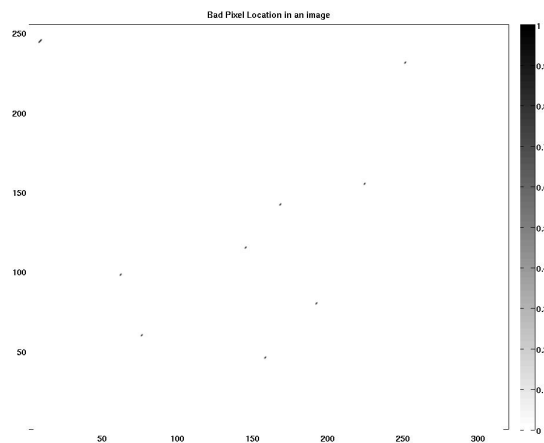


Figure 3.24: Location of the bad pixels

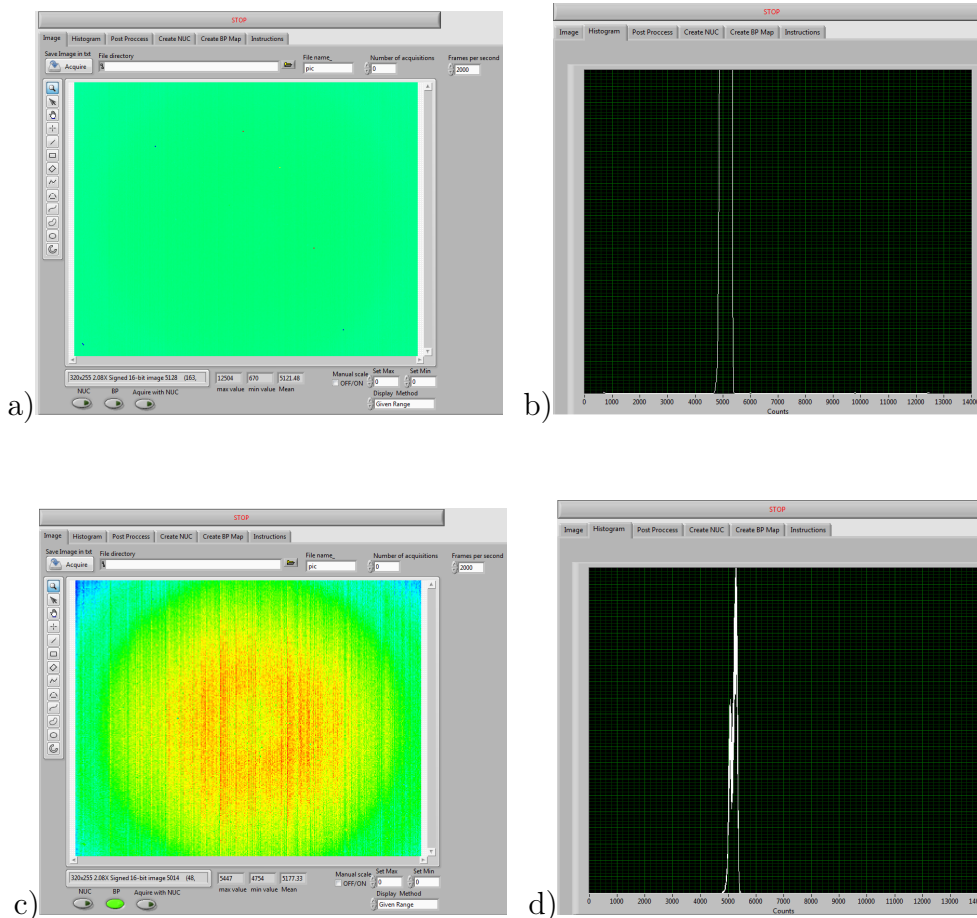


Figure 3.25: a) Picture with bad pixels b) Histogram with bad pixels c) Picture after removing the bad pixels d) Histogram after removing the bad pixels

Figure 3.25 a) and c) shows the improvement of the scale, since after removing the bad pixels the difference between the outliers decreases almost 11.000 counts.

2 Removal of the Temporal Noise

The LabView program to capture the pictures with the IR camera has as an input, frames per second. In order to check that the data is time independent, 1000 frames are collected and treated statistically to obtain the mean value of each pixel and, therefore discard variations and group them as an statistical error through the standard deviation. Figure 3.26 shows the idea.

The mean and the standard deviation are calculated and the same statistical procedure as the one shown in the bad pixel section is followed. All the images in the calibration and all the data acquired during the experiments, are approximated

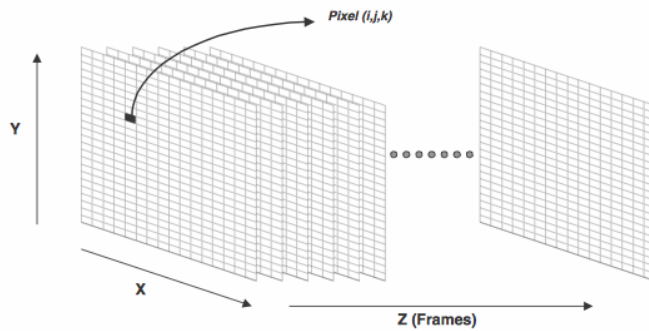


Figure 3.26: Frames to analyzed [16]

to the mean of 1000 frames. The temporal noise is assumed to be a Gaussian statistical distribution.

Figure 3.27 shows an example of how the value of the counts for the pixel placed in column 150 and row 150 is independent of time. This pixel was selected due to be placed near the middle of the image.

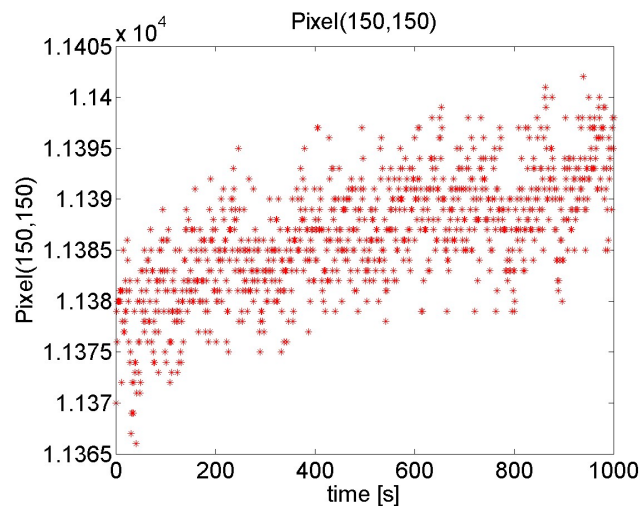


Figure 3.27: Pixel (150, 150) through 1000 samples at 59° used for the calibration

3 NUC

It is difficult to manufacture photo detectors with exactly the same response of electrical signal for the same input value. This problem is known as "non-uniformity" in IR technology and it manifests itself as superimposed grid in the output image of the camera, termed as fixed pattern noise (FPN). This noise emerges since the weak electric signals from the detectors must undergo a high gain amplifier stage,

thus magnifying their differences notoriously at the exit of the camera. To address this problem, the detector is characterized as a linear model with two parameters (gain and offset). The solution of this problem is called non uniformity correction (NUC).

The non-uniformity correction, must be able to meet the following requirements [3]:

1. All detector elements should produce signal values after correction with a minimum signal to noise ratio because of the low signal levels.
2. The correction must be effective throughout the signal range. Tolerable threshold non uniformity to be defined on a minimum threshold.
3. The method of correction must be compatible with their non-linear response of the FPA. Since usually linear tools are used, these non-linearities can lead to a correction that is not equally effective across the specified range. In an effort to resolve this situation is used to develop more sophisticated algorithms that require more computational effort.

In our work range, it is known that the camera sensors have a linear response. Therefore, doing a two point NUC must achieve requirements. In theory, it is not very complex to do a multiple point NUC and it is expected to acquire better results than using a two point NUC. Therefore, the three point NUC and the four point NUC were compared with the two points one, in order to check which case reaches highest uniformity levels. These points are uniform surfaces at different temperatures obtained with the calibration devices.

Once we have obtained the mean of the 1000 frames after the second step to correct the images we obtain the parameter \bar{Y}_{ij} . To remove the temporal noise the NUC theory is based on applying on each pixel (X_{ij}) in the matrix a gain (G_{ij}) and an offset (O_{ij}). The NUC made with n points is an application of the *Linear Least Square* method. The parameters are:

- n : Number of NUC points used in the interpolation.
- $Y_{ij}(n)$: Counts for each pixel after averaging 1000 images.
- X_{ij} : Counts for each pixel ij at n temperature image.
- G_{ij} : Gain for each pixel ij at n temperature image.
- O_{ij} : Offset for each pixel ij at n temperature image.
- $Y_{NUC,ij}$: New matrix made of corrected pixels ij .
- \bar{Y} : Spatial mean value of $Y_{ij}(n)$

-
- A , B and C : Auxiliary matrices.

Then the corrected image is obtained:

$$Y_{NUC,ij} = G_{ij} \cdot X_{ij} + O_{ij} \quad (3.3)$$

Where the Gain and the offset are calculated using the following equation:

$$\mathbf{A} = (\mathbf{C}^T \mathbf{C})^{-1} \mathbf{C}^T \mathbf{B} \Rightarrow \mathbf{A} = \mathbf{C}^+ \mathbf{B} \quad (3.4)$$

Where \mathbf{C}^+ is the **pseudoinverse matrix** of \mathbf{C} . In our case the matrices \mathbf{C} , \mathbf{A} and \mathbf{B} are defined as follows:

$$\mathbf{C} = \begin{bmatrix} Y_{ij}^{(1)} & 1 \\ \vdots & \vdots \\ Y_{ij}^{(n)} & 1 \end{bmatrix}$$

$$\mathbf{A} = \begin{bmatrix} G_{ij} \\ O_{ij} \end{bmatrix}$$

\mathbf{A} is an auxiliary variable which is the vector that contains the gain and offset that each photodetector requires. Finally, matrix \mathbf{B} is defined for this problem as:

$$\mathbf{B} = \begin{bmatrix} \bar{Y}^{(1)} \\ \vdots \\ \bar{Y}^{(n)} \end{bmatrix}$$

Thus, solving the system of equations can be found above the offset and gain matrices with which the correction is made.

Figure 3.28 shows the difference of a picture before and after the correction NUC with the value $n = 2, 3$ and 4 . Our human eye is unable to detect which value of n is the optimal. Therefore a comparison between the values of a pixel row at a uniform temperature was made. The outcomes for the standard deviation are:

Std(2points)=0.701

Std(3points)=0.5543

Std(4points)=1.0708

This minimum value for the standrad desviation and Figure 3.29 proves that the three points NUC achieve the most uniform response.

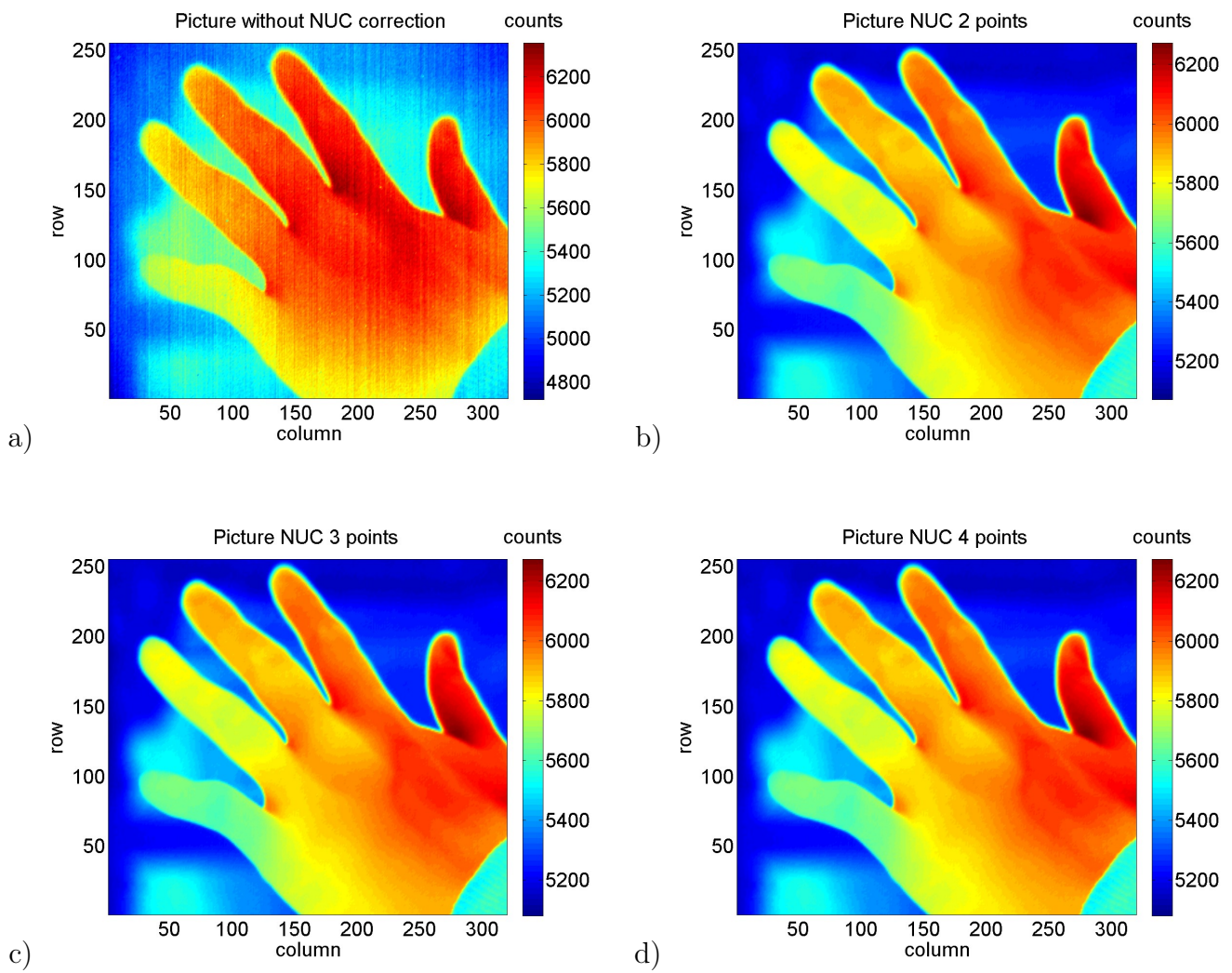


Figure 3.28: a) Picture before the NUC correction b) Picture after two point correction NUC
 c) Picture after three point correction NUC d) Picture after four point correction NUC

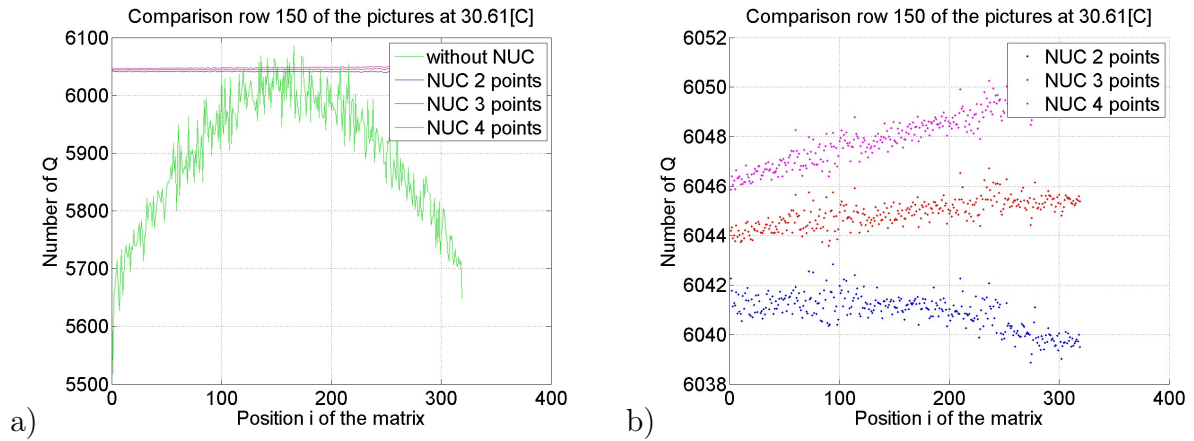


Figure 3.29: a) Counts of pixel row 150 before the correction b) Counts of pixel row 150 after the correction with different NUCs

To sum up, in order to perform a multiple point NUC a linear system has to be solved as many times as photo-detector exists in the system using the least interpolation method. Afterwards, a matrix of gain (G_{ij}) and offset (O_{ij}) is applied to each pixel. This algorithm has been performed using MatLab and the best results for the correction are given by three-point NUC ($n = 3$) shown in Fig. 3.30.

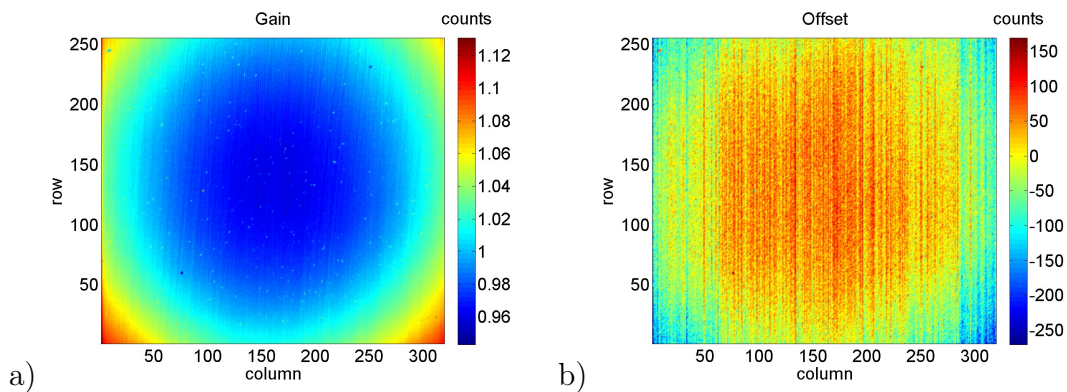


Figure 3.30: a) Gain b) Offset

3.4.3 Calibration

The data acquired with the IR camera are stored as 256x320 matrix of numbers. These numbers are counts measured by the photo-detector and they represent the thermal radiation of each pixel. A Matlab software is used to convert these measurements into temperatures. A polynomial obtained using least square interpolation is used for calibration purposes. Hence, the camera is calibrated with 5 uniform temperatures to generate a fourth or lower grade polynomial of interpolation. A program called RCal could perform the same calculation, but it is faster and more convenient if all the post process is managed in the same script of Matlab. However, RCal is very useful to check the results of the approximation as shown Fig. 3.31 a). The inputs are the five temperatures, the ε and the σ_r . According to the Planck's equation (Equation 2.2) in the wavelength interval that the camera works, the coefficients to obtain the radiation are calculated. Then the last step is converting the radiance into temperature.

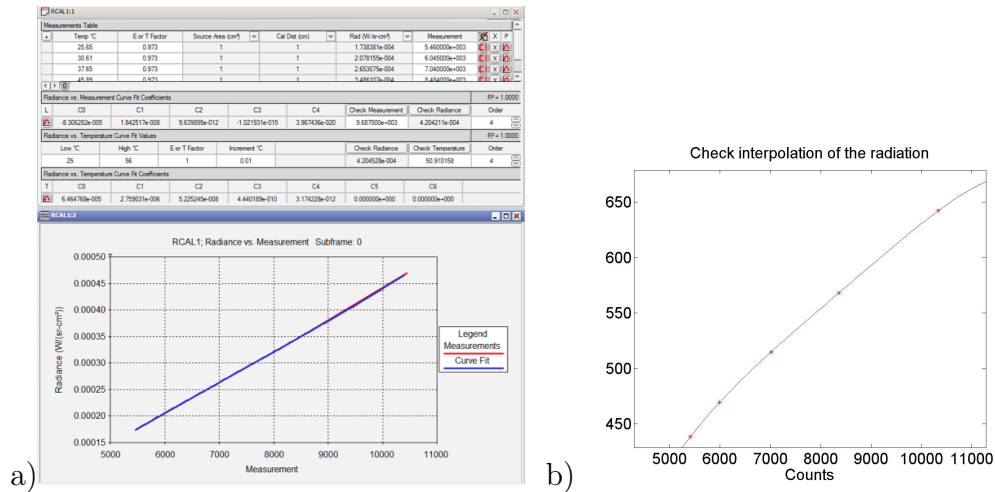


Figure 3.31: a) RCal calibration program b) Conversion into temperatures with Matlab

This process is performed after the image correction, obtaining an array of matrices of radiation coefficients which afterwards are transformed to temperatures.

3.4.4 Post processing to obtain the temperature map of the side wall

All the images are post processed and stored as a profile file in order to calculate in Fluent the HTC (a 3D mesh is used for this proposes).

After applying all corrections mentioned in this section, we obtain a temperature color map of one sector of the endwall (as shown in Fig. 3.32).

In order to calculate the temperature difference, three silver points were drawn to transform column and row information of each pixel to physical coordinates in a reference system of interest. The origin of the reference system is located at the down left corner of the endwall and the main axes are collinear with the edges of the endwall. The result of this procedure can be seen in Fig. 3.32. The black points in Fig. 3.32 represents the location of the 21 Pt 100.

In order to remove the wrong data obtained from the pixels affected by the markers, an interpolation algorithm will fill these pixels with a linear interpolation from the surrounding pixels which provide the right measures. The program gives an output image like the one shown in Fig.3.32.

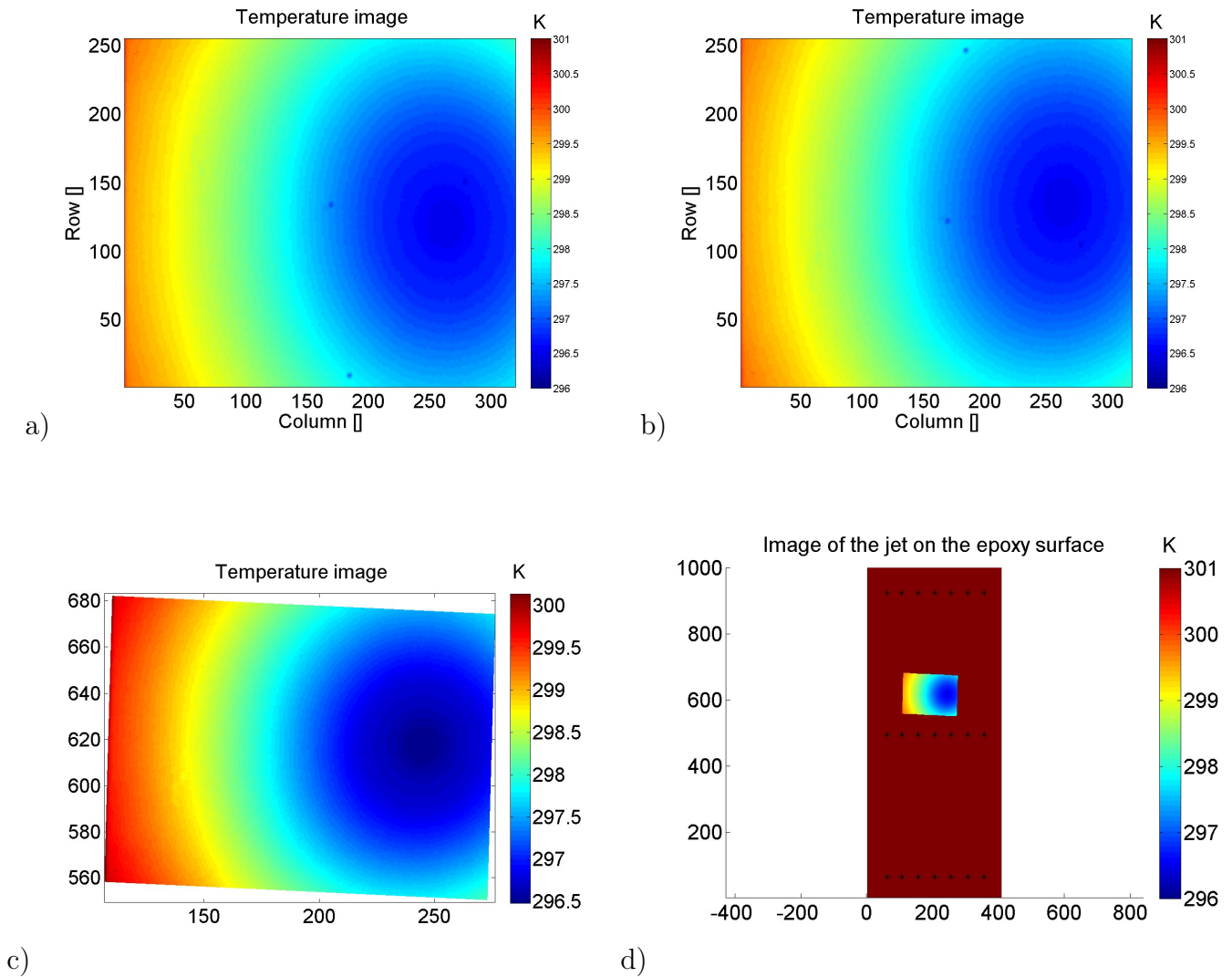


Figure 3.32: a) Picture of the jet b) Picture of the jet after flip c) Picture after removing the three points and with the new coordinate system d) Picture of the jet located on the endwall

Figure 3.32 is an example of the post processing for the jet experiment. The same procedure is carried out for the flat plate and OGV cascade cases.

The last step to obtain the temperature over epoxy surface, in the case of the OGV and flat plate cases, is based on a filter to remove the blue frame (see Figure 3.33) which is the part of the Plexiglass' small window frame inside the field of view of the camera. This filter is important since the range of the colors change automatically and the movement of the flow and the variation of temperatures can be visualized by the outcome picture (Fig. 3.33).

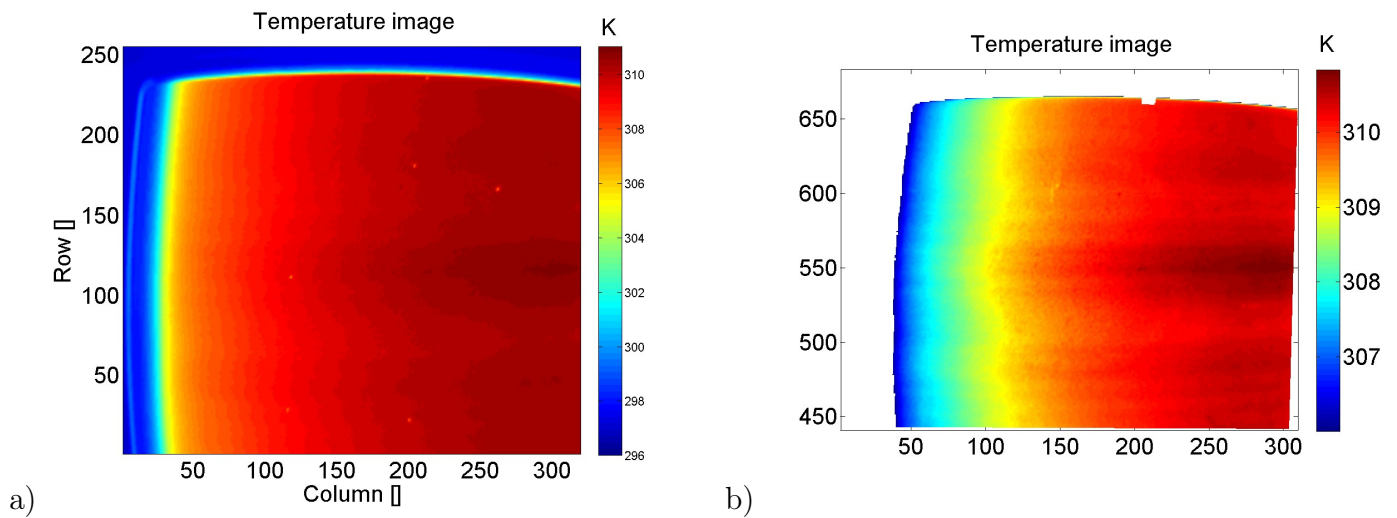


Figure 3.33: a) Epoxy temperature distribution for the flat plate with the window frame b) Epoxy temperature distribution for the flat plate after the filter process

Chapter 4

Heat transfer experiments

This part of the report explains the heat transfer experiments. In the first one the flow generator is a compressed air system that supplies air at the required Reynolds number at the outlet of a long nozzle so that a developed flow is obtained. Afterwards, the linear cascade rig located in Chalmers University of Technology is used to study the flat plate. The experiment in the linear cascade would be compared to previous results in experiments already carried out in our division. Different equations to calculate the HTC are required for the experiments since the flow have different characteristic, starting from the fact that the jet flow is compressible and the linear cascade flow is incompressible. When the flow is incompressible and there are no large changes in temperature, we can assume that the density of the air is constant. The area affected by impinging jet is smaller than the area of the epoxy on the endwall, while the linear cascade cools down the entire endwall and in a more uniform way. These factors will be appreciated in the results.

4.1 Jet impingement

This experiment is performed to study the effect of a steady impinging jet on the smooth and flat endwall. The air flow is turbulent, and the velocity profile at the outlet of the nozzle is fully developed. A single jet from a straight circular nozzle of length to diameter ratio (l/d) of 83 is tested. Reynolds number based on nozzle exit condition is varied between 15.000 and 36.000 and distance from the jet exist to the wall changed between 6 and 8 nozzle diameters.

The local heat transfer characteristics are evaluated using thermal images obtained by infrared thermal imaging technique. The local heat transfer distributions are analyzed based on theoretical predictions and experimental results of the fluid flow characteristics in the various regions of jet impingement. The heat transfer in the

wall jet region is studied considering fluid flow over a flat plate of constant heat flux as it is explained in the Theoretical Background. Correlations for the local Nusselt numbers in different regions are obtained and compared with experimental results [9].

It is known that fluid flow behaviour over a heated surface dictates convective heat transfer characteristics. The calculation of *HTC* and *Nusselt* number shown are based on regression analysis from experimental data. The guide of the jet experiment is :

1. The purpose of the experiment is to achieve the convection heat transfer coefficient over the heated endwall surface mainly in the area where the jet impacts. The expected results from the experiment carried out are associated expected accuracy and precision developed in detail in Chapter 3.
2. The measures needed are:
 - (a) The temperature distribution of the aluminium surfaced, measured with 21 thermocouples Pt 100. Section 3.3
 - (b) The temperature distribution of the epoxy surface, obtained with an IR camera. Section 3.4
 - (c) Mass flow and pressure.
3. The outcomes after the required post processing of the data and calculations are the *HTC* and the *Nusselt* numbers.
4. To validate the design by performing analysis of the result as discussed in Chapter 6.
5. Repeat the process with the flat plate case in the linear cascade facility.

4.1.1 Experimental set up

The epoxy surface 414x990mm of the endwall is pointed with the IR camera and with the nozzle. Both devices are supported very carefully to avoid any vibration or movement. The holder is based on metallic structure as Figure 4.2 shows. The range of the power supplied to the heaters is between [137 W - 140 W].

The isothermal flow is transported by a hose from an outlet of air under pressure to the endwall. The pressure at the inlet to the mass flow meter is monitored with a barometer and controlled with a manual valve. This is important due to the second manometer has a maximum pressure value of 3bar. The flow meter used has as maximum value of 209.84 L/min after. This quantity of volume flow rate is

required to achieve the highest Reynolds number studied in the experiment. It is expected that the temperature of the jet and the ambient temperature would be the same, nevertheless due to the fact that the temperature has a very important role in the equations it would be measured with a Pt 100 resistive thermometer.

The whole endwall piece is explained in detail in section 3.1.

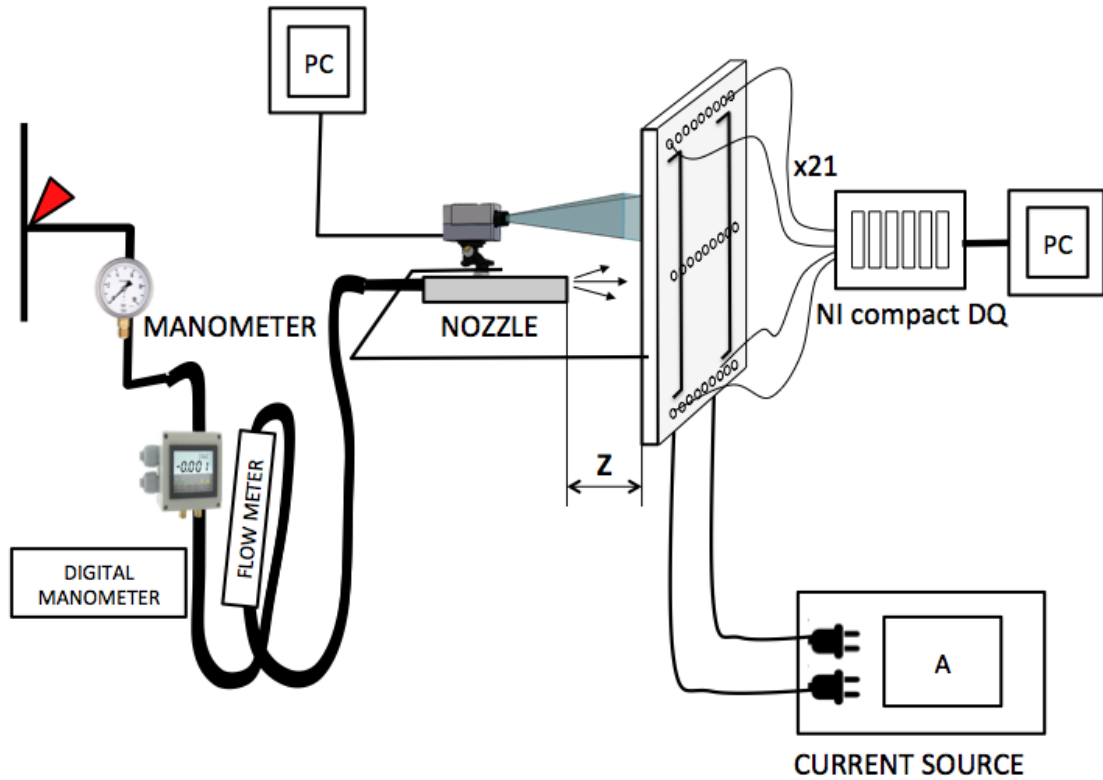


Figure 4.1: Set up for the impinging jet experiment

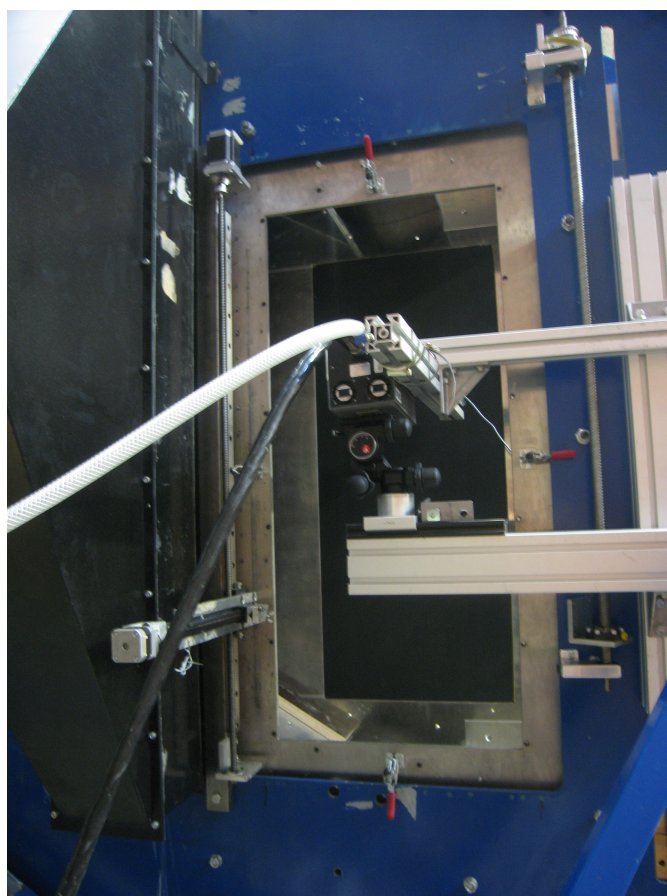


Figure 4.2: Epoxy surface of the endwall pointed with the IR camera and the jet

4.2 linear cascade

The linear cascade is located at Chalmers University of Technology. The main purpose of having such facility is to study the flow around outlet guide vanes and to provide CFD validation data for 2D and 3D geometries. Since the OGVs are located at the outlet of the LPT, they should stand different inlet angles minimizing the aero losses and standing the aero and thermal loads.

The facility (Figure 4.3) consists of a centrifugal fan (30 kW), a wide angle diffuser, a settling chamber where the outlet flow does not contain wakes which were generated on the centrifugal fan, a rectangular contraction section and a test section with boundary layer suction [14]. The testing area of the linear cascade, where the vanes are placed has a cross section of $240 \times 1200 \text{ mm}^2$. In the test section there are located four OGVs and pitching an space between them of 240 mm. In order to

control the periodicity in the test section, there are two metal plates attached to the topmost and bottommost vanes to adjust the outlet section flow. Furthermore, the level of the incoming flow turbulence intensity is controlled by a turbulence grid which is located 700 mm upstream of the cascade. Also to ensure that the air flow is turbulent in the boundary layers, a vertical sand paper band with a width of 30mm is located at a distance of 210mm from the endwall (Figure 4.4). This information would be used for the correction of the *HTC* in the results. More details concerning the design of the linear cascade can be found in [7].

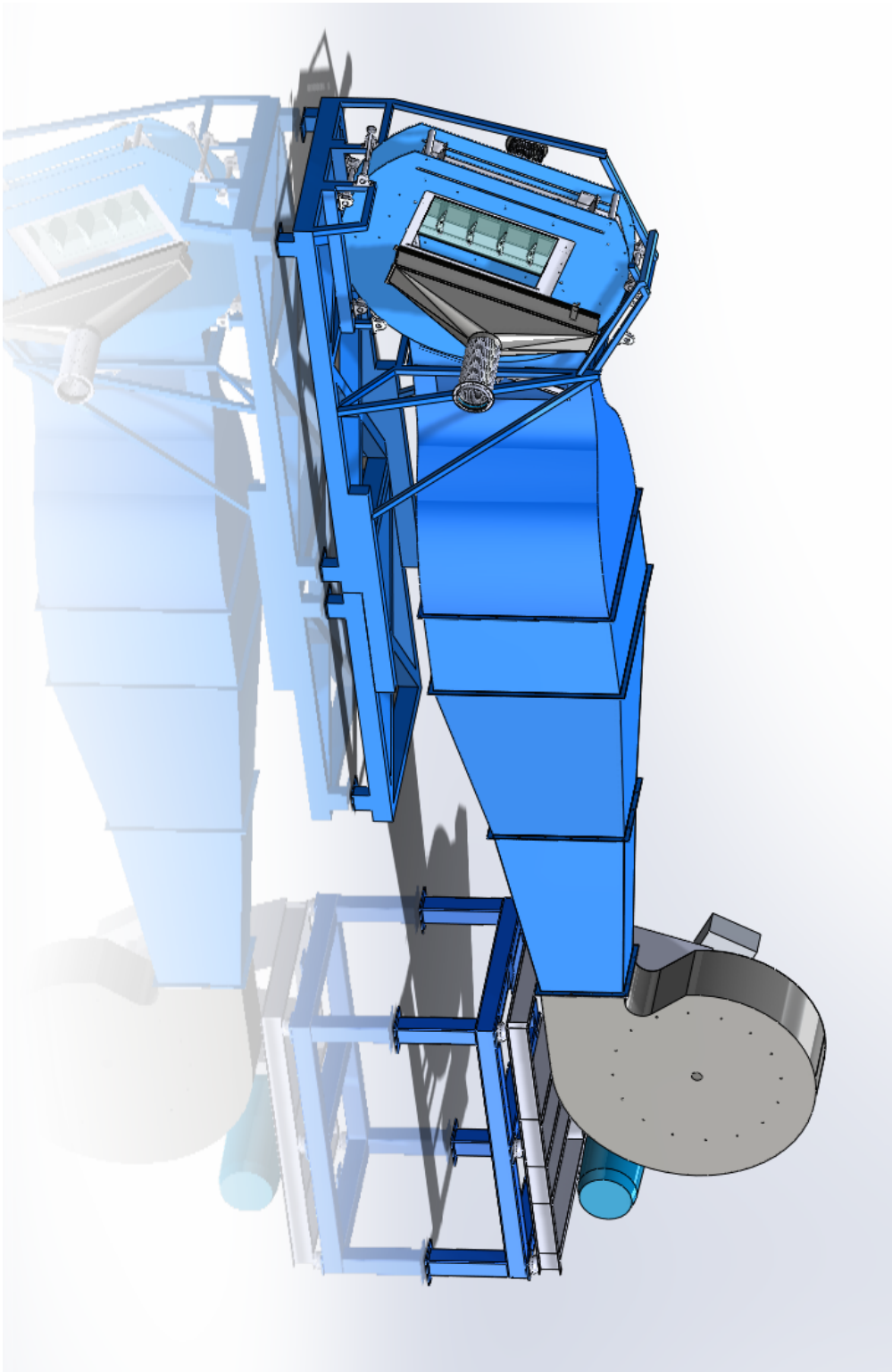


Figure 4.3: linear cascade

The angle of attack of the vanes is a variable to take into account for the flow measurements, for $\alpha = 0^\circ$ (on design case, 28.50° in our coordinates system) the heat transfer is higher [8]. The linear cascade allows the study of different operation points, air velocity and angle of vanes. In our case, the study is focused in three points (20 m/s, 25 m/s and 30 m/s for the air inlet velocity). For the study of the endwall as a heated flat plate the angle is 0° while for the OGV the linear cascade is in on-design position which means an angle of 28.5° . The power supplied to the heated wall is around 360 [W] in the different velocity cases. Applying this power, a wall temperature on the aluminium-epoxy interface of 55°C is obtained. It is critical not to exceed 60°C on the aluminium-epoxy interface since there is a risk that the epoxy would be detached from the aluminium due to thermal stresses.

The guide for the linear cascade experiment is :

1. The aim of the experiment is achieve the convection heat transfer coefficient over the heated endwall surface. First, the endwall has to be validated comparing the results with scientific papers covering the topic. Once is tested that the endwall behaves as expected, the vanes of the OGV are mounted to carry out the last measurements to understand the complex heat exchange taking place between the air the vanes and the wall.
2. The measures needed are:
 - (a) The temperature distribution of the aluminium core, measured with 21 resistive thermometers Pt 100. Section 3.3
 - (b) The temperature distribution of the epoxy surface, obtained with an IR camera. Section 3.4
 - (c) Pressure at different points of the linear cascade. Section 4.2.1
3. The outcomes after the required post processing of the data and calculations is the heat flux along the endwall.
4. To validate the design. Comparison and results are discussed in Chapter 6.
5. Follow the research introducing the vanes in the linear cascade and back to step 2. The research will be completed when these last results will be compared with the Fluent simulations.

4.2.1 Flow measurements

The inlet conditions of the low speed airstream is usually considered to be defined when we know the distribution of the temperature, pressure or velocity and turbulence. According to Bernoulli, the velocity of the fluids can be obtained from a

derivation of the principle of conservation of mechanical energy. The equation is:

$$P_t - P_s = \frac{1}{2}\rho v^2 \quad (4.1)$$

In order to use Bernulli's equation some assumptions are required as the flow that under study must be steady. Hence, the sum of all forms of mechanical energy in a fluid along a streamline is identical at all points. This involves the conservation of the energy therefore an increase in the pressures of the air brings an increase in the speed and vice versa.

Setting the speed of the linear cascade appears straightforward as we apply our basic understanding of fluid dynamics. However, it becomes complex due to inserting a pitot-static tube or other measuring device in the test section to measure dynamic pressure or speed of the flow will cause changes in the flow under study.

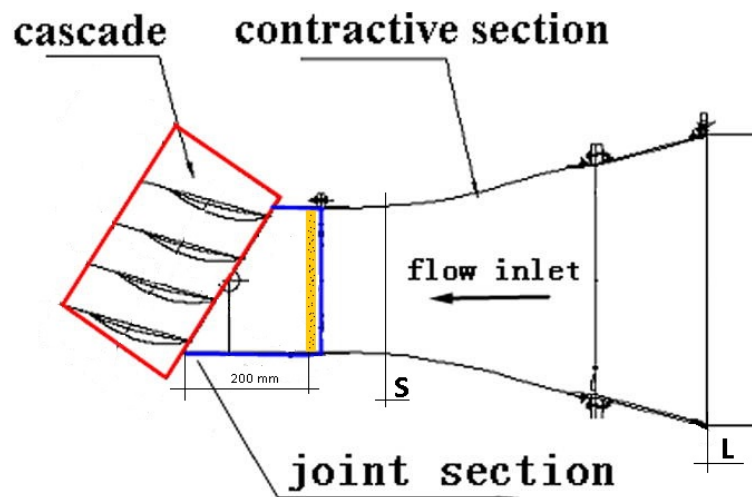


Figure 4.4: Linear cascade. Using in the text L for the bellmouth, S before the text section

Figure 4.4 shows how the section from the cone to the test section suffer a contraction. It causes an increase in the speed air flow. To counter this development two suctions(right and left) are installed in section S.

The dynamic pressure in the bellmouth (L) is called P_L and P_S is the dynamic pressure before the test section [1]. The calibration of the test section should be based on running the linear cascade at various values of $P_L - P_S$ while measuring the dynamic pressure in the test section with a calibrated Pitot-static tube. But due to difficulties in the accessibility in the linear cascade just a Pitot tube is

installed in section S, we assume that the velocity profile is not fully developed and it is going to be characterized for its parabolic shape.

To obtain the optimal working point per each pressure drop, the intensity of the suction can be regulated looking at the panel displayed in Figure 4.5. Once the pressures are stabilized the suction is controlled to the highest similitude between the pressures at the right side of the linear cascade represented by channels 1-5 and the left side (channels 11-16).

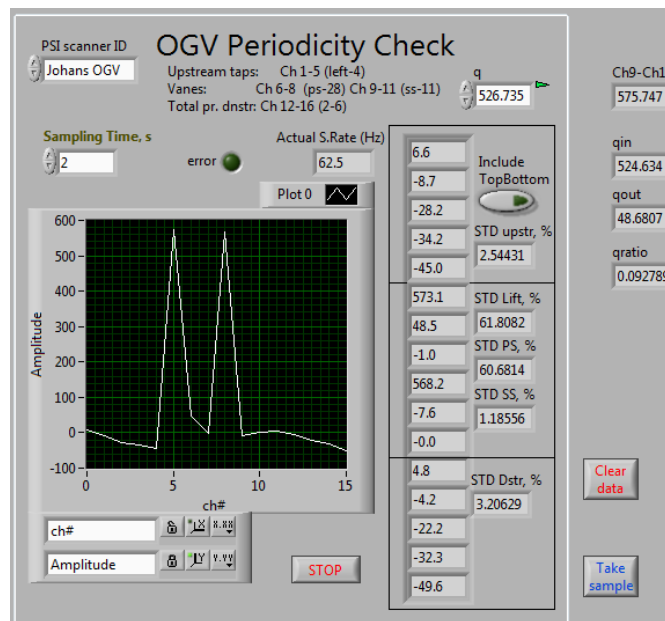


Figure 4.5: Pressure control of the flow in the linear cascade

The input speed for the flow is controlled with a power inverter. The velocities under study are 20 m/s, 25 m/s and 30 m/s. The air flow for the experiments, according to the Mach number ($M = \frac{v}{v_s}$), is incompressible. This is because $M < 0.3$. In the Mach number v is the velocity of the air flow and v_s is the velocity of the sound in the medium.

The boundary layers involved in the linear cascade are generally much thicker than those encountered on a real geometry at realistic condition [1]. They can be measured with a traversing system device fitted with a Pitot tube coupled to the linear cascade as can be seen in Figure 4.6.

In order to generate a physical for the traversing system to take the measurements, a Matlab script has been created. Figure 4.7 shows this path and indicates the

axes and the orientation that are going to be taken as reference.

All the boundary layers are turbulent due to the fact that two coarse sandpaper films are glued to the wall upstream the test section. All the pictures of the boundary layers, velocity maps and pressure maps can be found in the results section. Figure 4.8 shows the effect of having 2 different operating points in the suction system for the same velocity inlet into the test section. Hence, prior to start measuring the HTC with the heated endwall and IR camera, the flow inside the linear cascade had to be measured and regulated. The information of the boundary layer will be used for the correction of the HTC it is explained in Chapter 6.

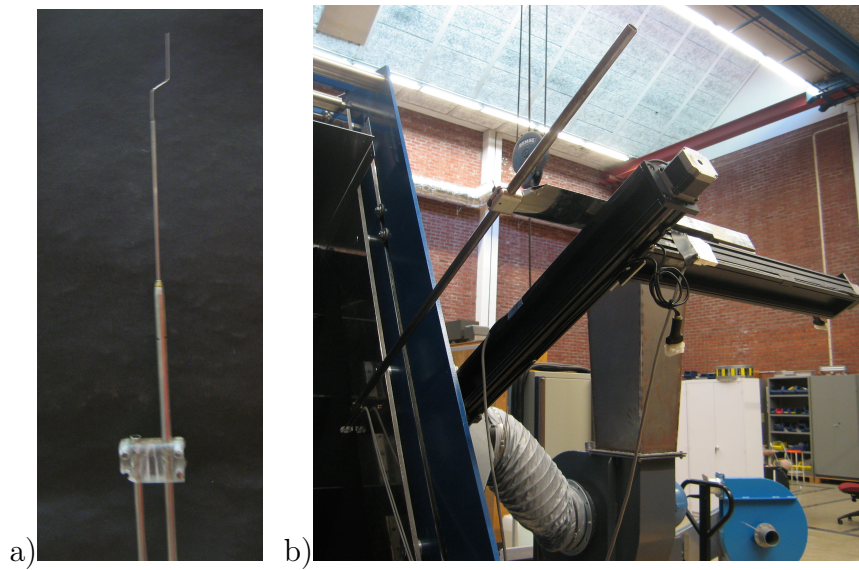


Figure 4.6: a) Pitot tube used to measure the boundary layer b) Traversing system coupled to the linear cascade

Path of the traversing system close to the wall

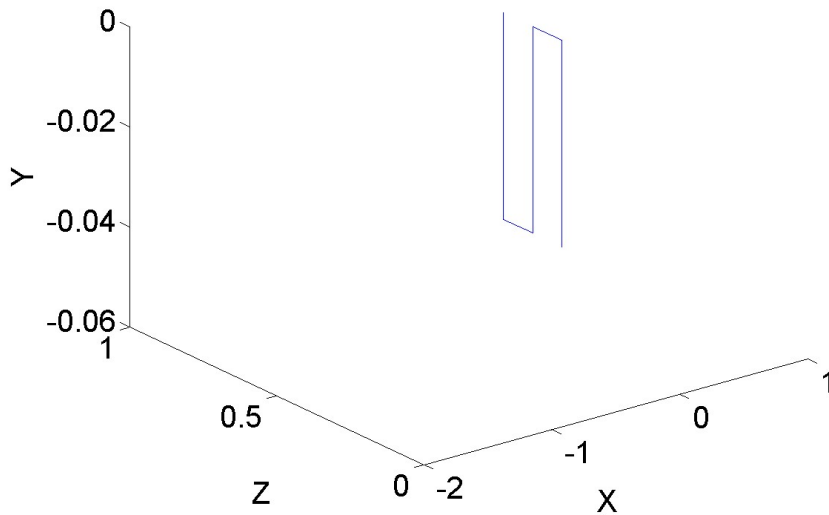


Figure 4.7: Path followed by the traversing system to measure the boundary layers

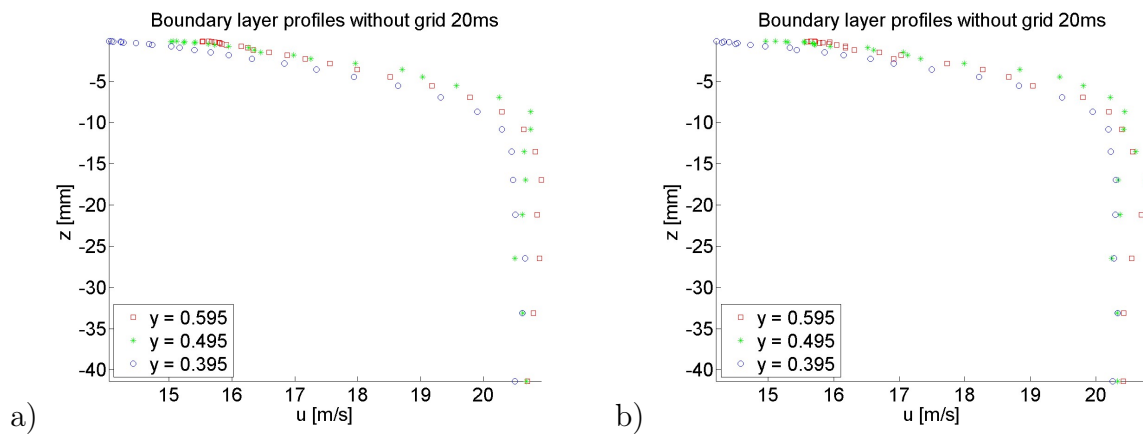


Figure 4.8: Velocity profile measured close to the wall at 20 m/s. Suction supplied by an electrical motor rotating at: a) **25Hz** and b) **40Hz**

Chapter 5

Calculation of the Heat Flux in the Endwall

Once the temperatures of the aluminium surface (section 3.3.4) and the epoxy surface (section 3.4.4) have been acquired and saved as a .txt and .prof file. The HTC can be calculated following two different procedures:

1. A 3D model simulation in Fluent.
2. A 1D model in Matlab.

Both models perform calculations according to the heat transfer equations. While in Fluent a 3D temperature gradient calculation can be calculated numerically, in Matlab only the gradient perpendicular to the epoxy surface is calculated. However, they share the boundary conditions and reference values for all the domain (see Table 5.1).

As it has been explained in Chapter 4.1 the *HTC* and therefore the Nusselt number for the **jet experiment** are dependent on the distance to the stagnation point. Then, in order to visualize the temperature and HTC distribution for this experiment, all the data must be referred to the stagnation point. The values will vary with the radius and the angle. This is obtained with a Cartesian to polar coordinates system transformation. One of the images obtained from these experiments is shown in (Fig.5.1).

In the other cases, after post processing the pictures, the information obtained is exported to the CFD software FLUENT. Using this software, the temperatures measured on the surface with the IR camera are set as a boundary condition over the epoxy surface and the interpolated temperature distribution over the aluminium-epoxy interface is set in Fluent as boundary condition. The temperature of the air is also a parameter set in Fluent. Hence, when all the boundary conditions and the material properties are fixed the *HTC* is calculated over all

Parameter	Value	Description
ε	0.973	Emissivity of the coated epoxy surface.
σ	$5.67 \cdot 10^{-8} [\frac{W}{m^2 K^4}]$	Stefan-Boltzmann constant
k_{epox}	$0.2 [\frac{W}{mK}]$	Thermal conductivity of the epoxy.
t	5 [mm]	Thickness of the epoxy.
k_{air}	$0.0259 [\frac{W}{mK}]$	Thermal conductivity of the epoxy.
T_{amb}	[K]	Room temperature of the test day.
T_{epox}	[K]	temperature of the epoxy surface.
$T_{aluminum}$	[K]	temperature of the aluminum surface.
v	[20-30] [$\frac{m}{s}$]	Velocity of the air flow (linear cascade).

Table 5.1: Inputs required for the *HTC* evaluation

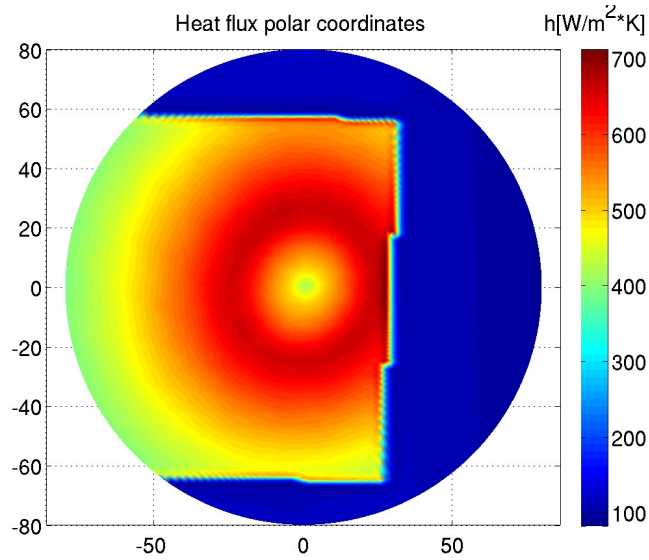


Figure 5.1: Picture of the jet polar coordinates

the studied surfaces applying the theoretical model described in the theoretically background.

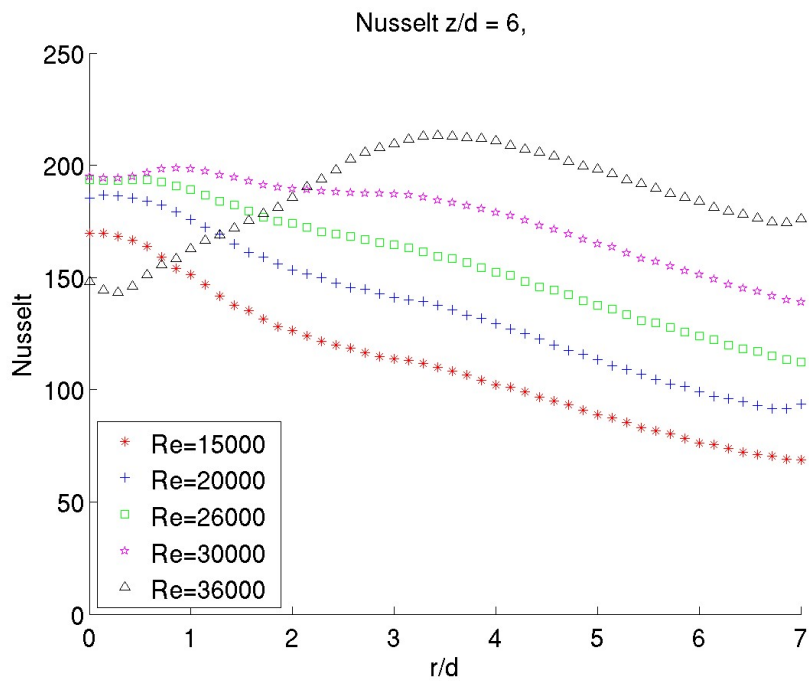
Chapter 6

Results

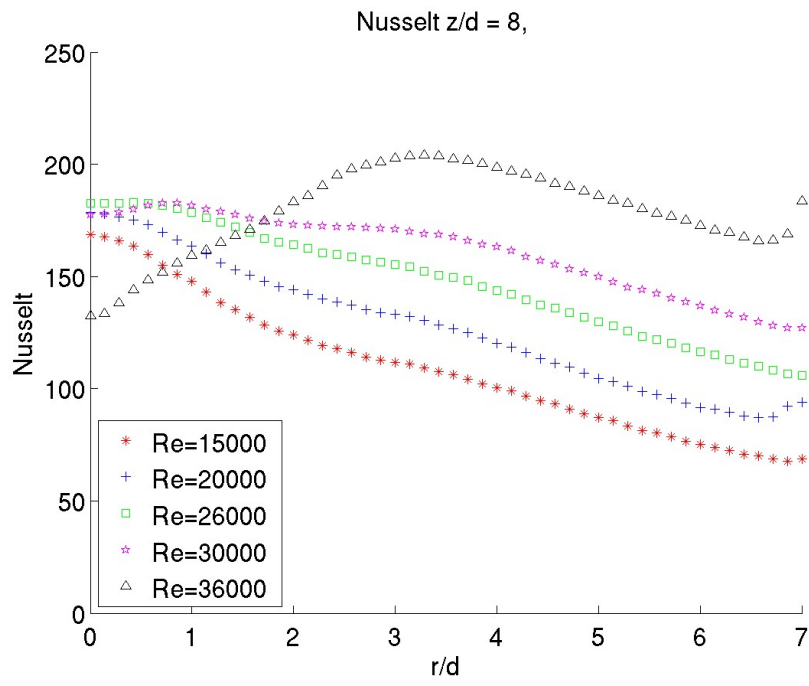
6.1 Results for the jet impingement case

Local heat transfer distribution is measured for different jet to plate spacings (z/d), 6.0 and 8.0. In addition for each jet to plate spacing ratio the Reynolds numbers has been set to 15.000, 20.000, 26.000, 30.000, 30.000 and 36.000.

For all Reynolds numbers with the exception of $Re = 15.000$, it is seen that the Nusselt number decrease when the distance from the nozzle to the plate is increased from 6 to 8. It was expected following previous researches as [9] and [12]. Figure 6.1 shows than the Nusselt tendency monotonically decreases in the radial direction away from the stagnation point. However, from a Reynolds number of 26.000 and higher, transition phenomena has been detected. The tendency of the lines are similar per the different values of the Reynolds number when the parameter z/d changes. Compared with existing experimental data provided in [9] or [12], The Nusselt number in all the cases is higher than expected in all the domain, but obtaining worst comparison in furthest area from the stagnation point.



a)



b)

Figure 6.1: a) Nusselt $z/d = 6$ b) Nusselt $z/d = 8$

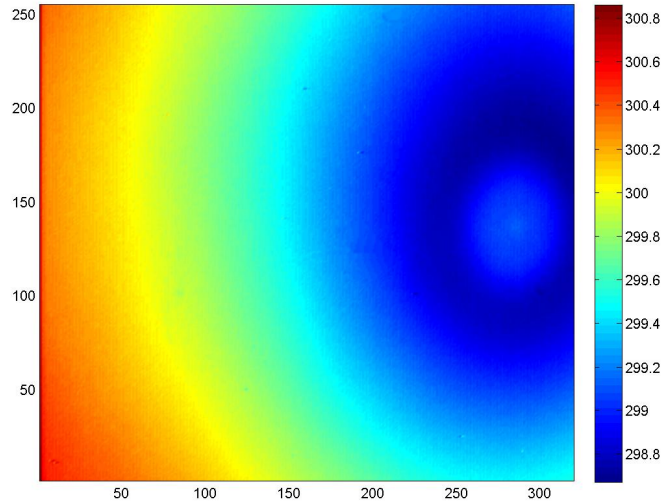


Figure 6.2: *HTC* color map of the case $z/d = 6$ at $Re = 36000$

It is concluded that the endwall has not been design to calculate local heat transfer coefficient, when a jet is impinging in a small section of the entire surface. The air jet does not cover the total heated endwall, reason why the heat supplied for the heaters can not be distributed uniformly along the layers of the endwall. In addition an other source of error in this experiment is that the temperature difference between the epoxy surface and the air flow is lower than 2°C . The nozzle was not instrumented to obtain a reliable temperature reading. Locating a Pt 100 at the outlet of the jet was not providing an stable value for the temperature. The oscillation were around 0.4° . If in the future a new experiment campaign is performed with this endwall and this kind of flow, locating a temperature sensor inside the nozzle in a steady position and isolated external influences will be critical. It was at this point that it was decided to follow the research in the linear cascade facility.

6.2 Results for the flat plate case

Three cases are under study for the validation of the endwall, 20 m/s 25 m/s and 30 m/s. First it was required to calculate the velocity profile and the boundary layer thickness per each velocity, in order to introduce the correction for the values of the *HTC*. This correction is required since in this case there is an unheated wall distance. The test section, where the heated endwall is located, starts at $x = 0$ but the distance from the suction system, from where the boundary layer

starts to develop, is 210 mm. There are two sand paper bands in the wall downstream the suction system to guarantee a turbulent flow. The correction of the HTC number is based on the development of the boundary layers. If this number is not corrected a drop in the values for the first 50 mm of the endwall would be appreciated.

Another improvement applied is the X^2Y^2 interpolation, not only to obtain the entire aluminium surface but also between the values of the temperatures measured with the Pt 100. Figure 6.5a shows this interpolation with the dot lines. When these interpolations are included, the values of the HTC in the first and last 50 mm of the endwall are corrected, resulting in the blue line with a concave curvature along the width of the endwall (see Fig. 6.7). The problem is that the value of the 6 Pt 100 located in the right and left sides is lower because of this Pt 100 are not completely immersed inside the holes due to the shape of the aluminum core. Hence, the Pt 100 are in contact not only with the aluminium but with the insulating material as well. This fact changes the measure of the temperature, reading a lower value as expected.

The experiment for the validation is carried out without the turbulence grid to compare with the correlations explained in the background from Incropera [11]. Furthermore, according to Volker [12], the open grid area is a parameter of second order and the vortices generated by the grid. They can be visualized for the case with the vanes, but it is inconvenient to study how the flat plate behaves towards validating with existing correlations from Incropera [11].

The view of the velocity profiles show better the difference between running the linear cascade with or without grid, Figure 6.4 shows that the velocity profiles are very similar with and without grid.

The HTC values are expected to be higher with the grid since more turbulence means an increase in the heat transfer coefficient. It is proved in the figures of the HTC values when the vanes and the grid are installed (see Section 6.3). In the boundary layer plots, the different dot lines represent the boundary layers for different endwall heights. The green one will be selected in all the cases, the argument for this decision is based on the fact that due to the geometry of the suction, it is more efficient in the middle of the suction duct inlet, which corresponds to $y=495$ mm.

Figure 6.3 and 6.4 show a study case where the inlet velocity is equal to 20 m/s. When the velocity is increased, the boundary layer decreases as it was expected, from $\delta = 6.94\text{mm}$ at 20 m/s to $\delta = 6.84\text{mm}$ at 30 m/s.

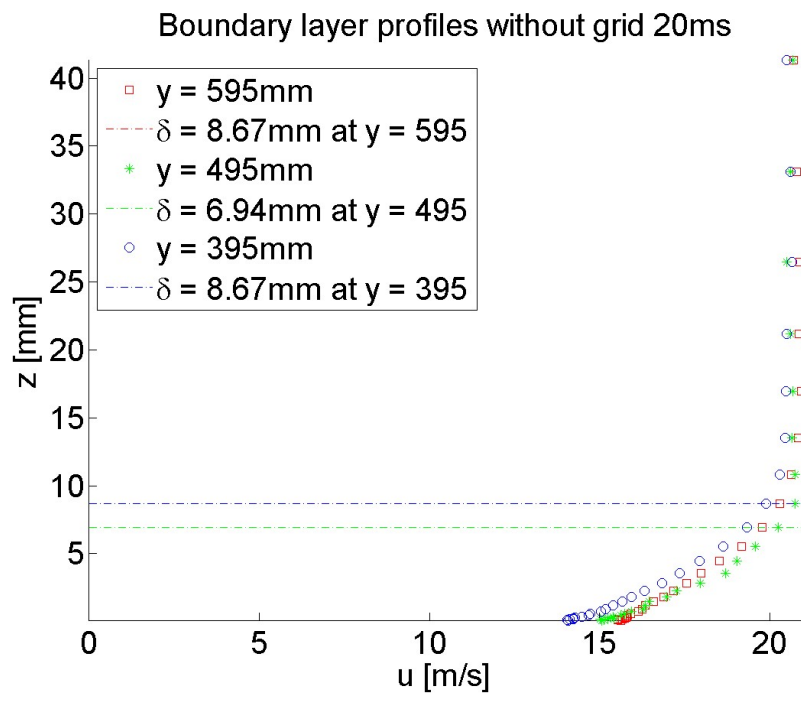
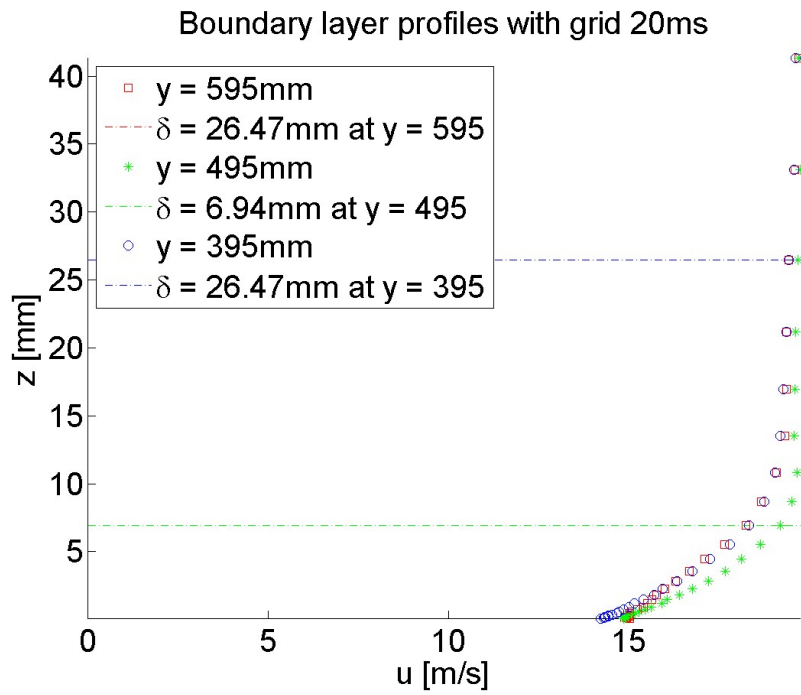


Figure 6.3: a) Boundary layer when the grid is located upstream b) Boundary layer without grid

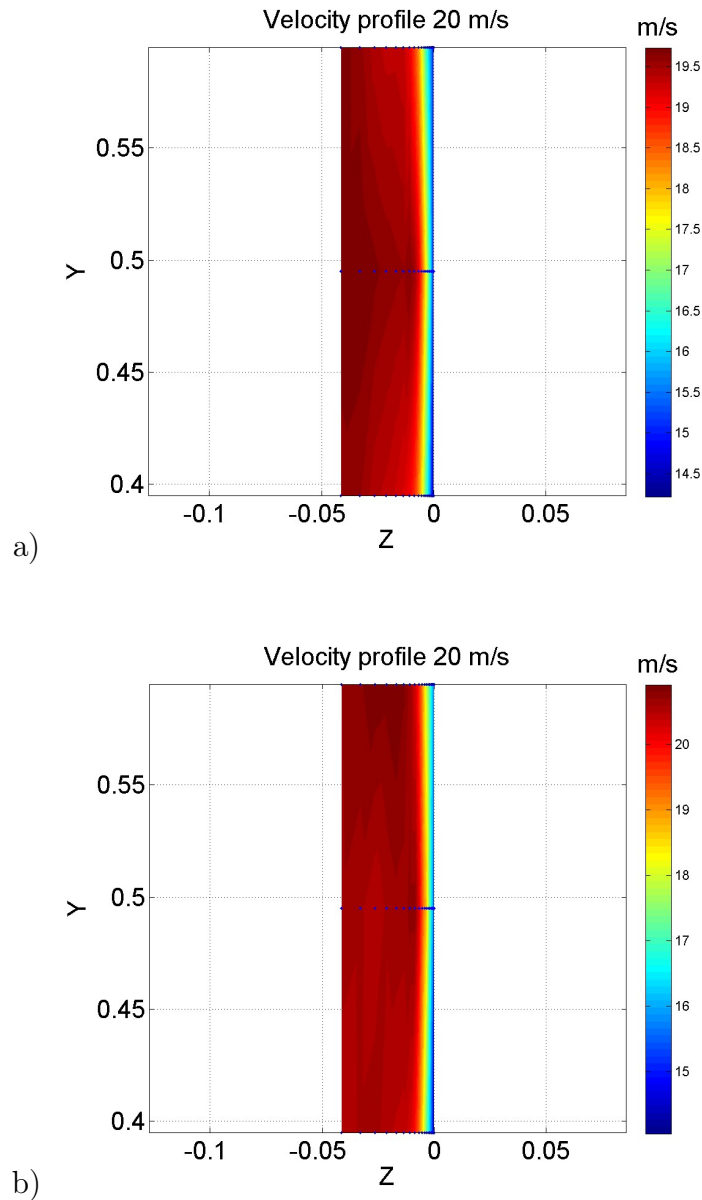


Figure 6.4: a) Velocity profile when the grid is located upstream b) Velocity profile without the effect of the grid

It is assumed that the temperatures are constant in time. In the aluminium-epoxy interface, this is checked calculating the variation of the Pt 100 measures in relation to the average. While for the epoxy surface, it has been measured a maximum variation of 0.15°C . The following figures 6.7, 6.8 and 6.9 shows the entire post processing and the outcomes and the values of the HTC at 20 m/s followed by the HTC results at 25 m/s and 30 m/s.

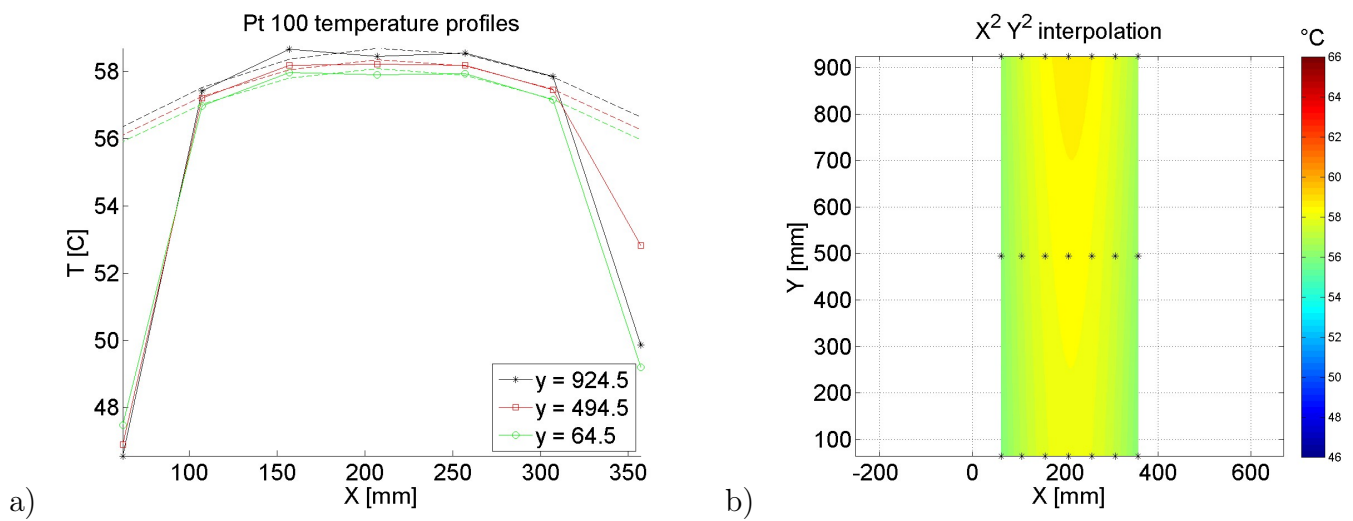


Figure 6.5: a) Pt 100 temperature profile of the aluminium b) Temperature distribution of the aluminium surface

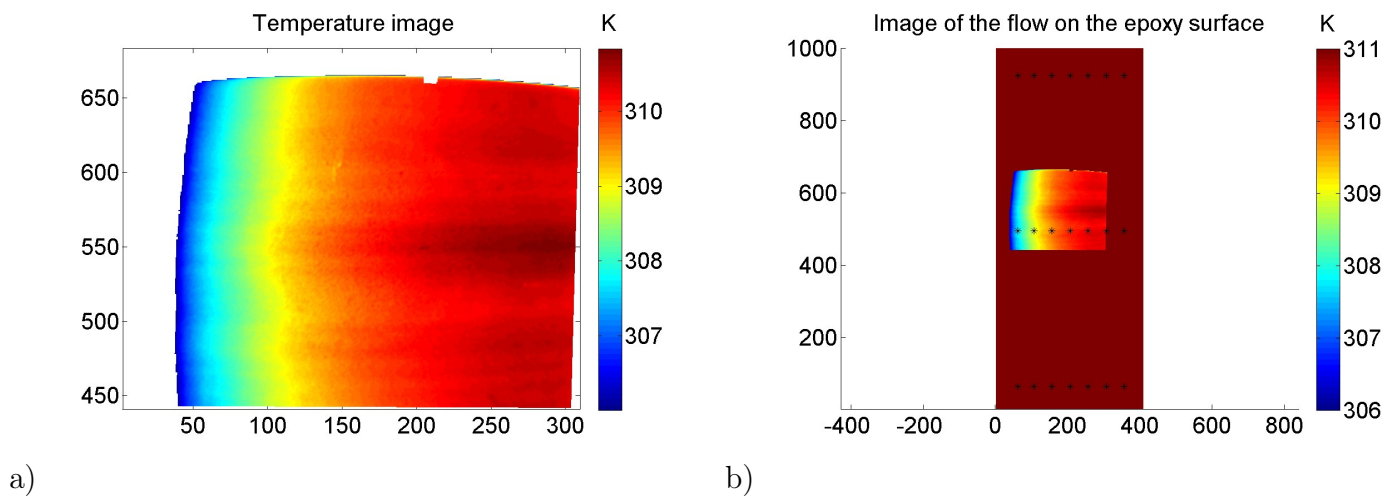


Figure 6.6: a) Temperature of the epoxy b) Temperature of the epoxy located in the endwall

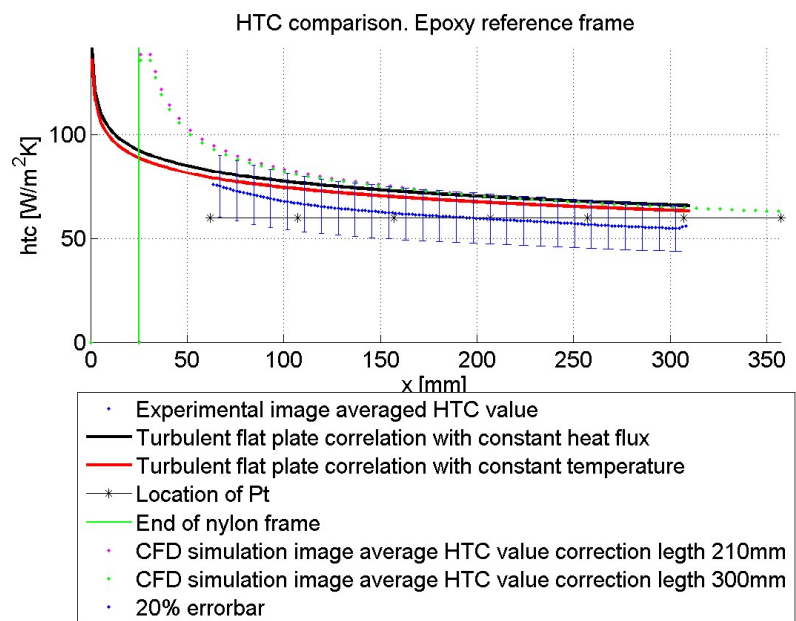
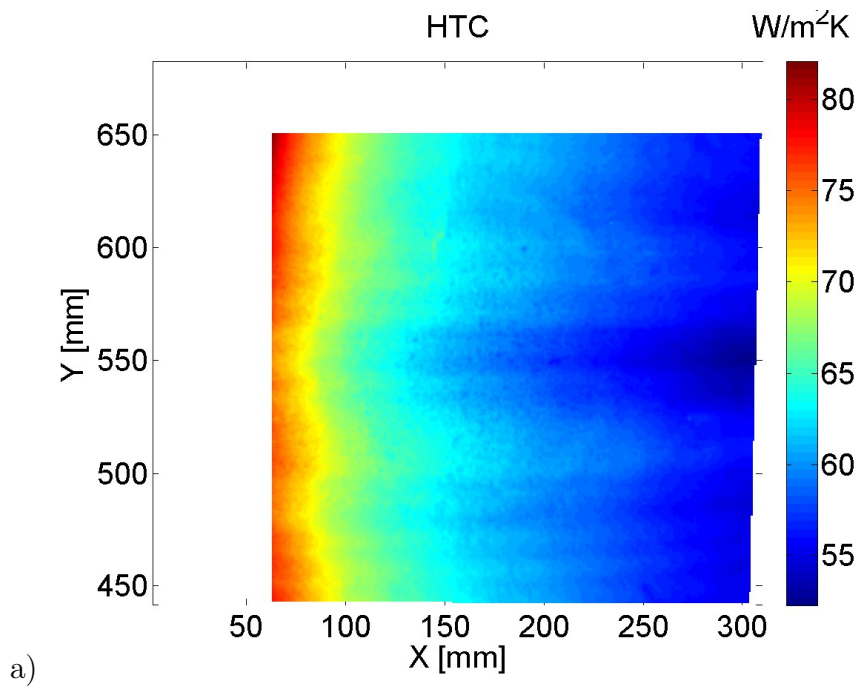


Figure 6.7: a) *HTC* at 20 m/s color map b) Averaged *HTC* at 20 m/s

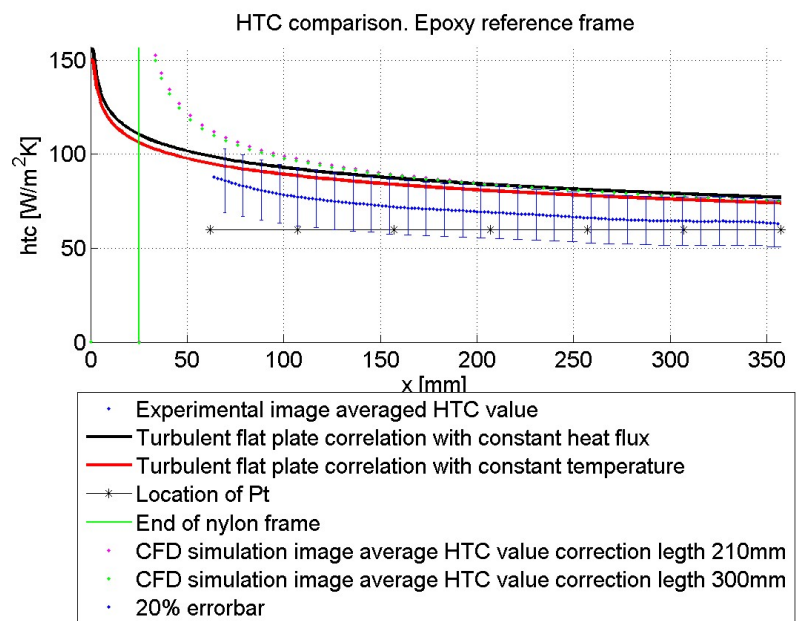
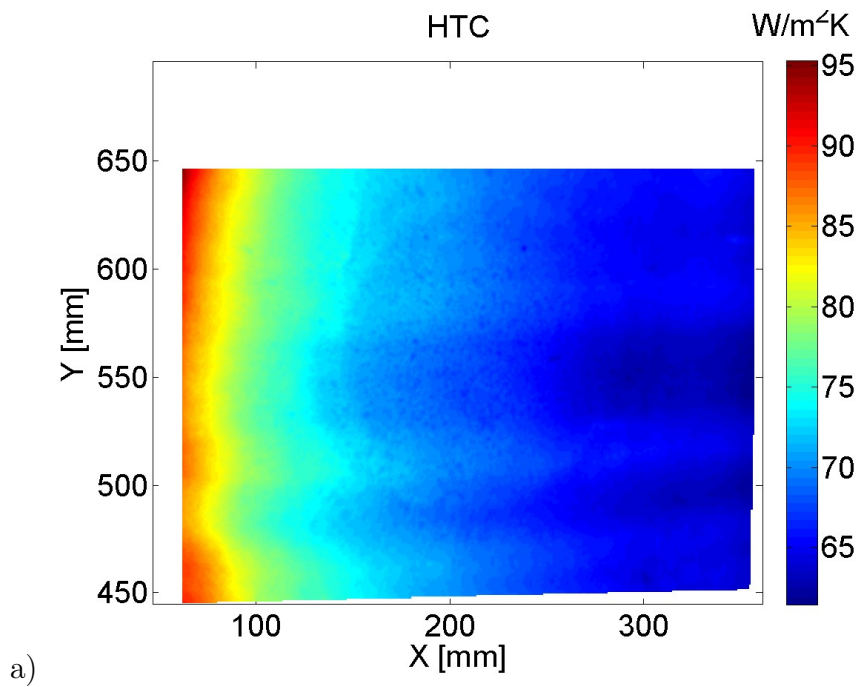
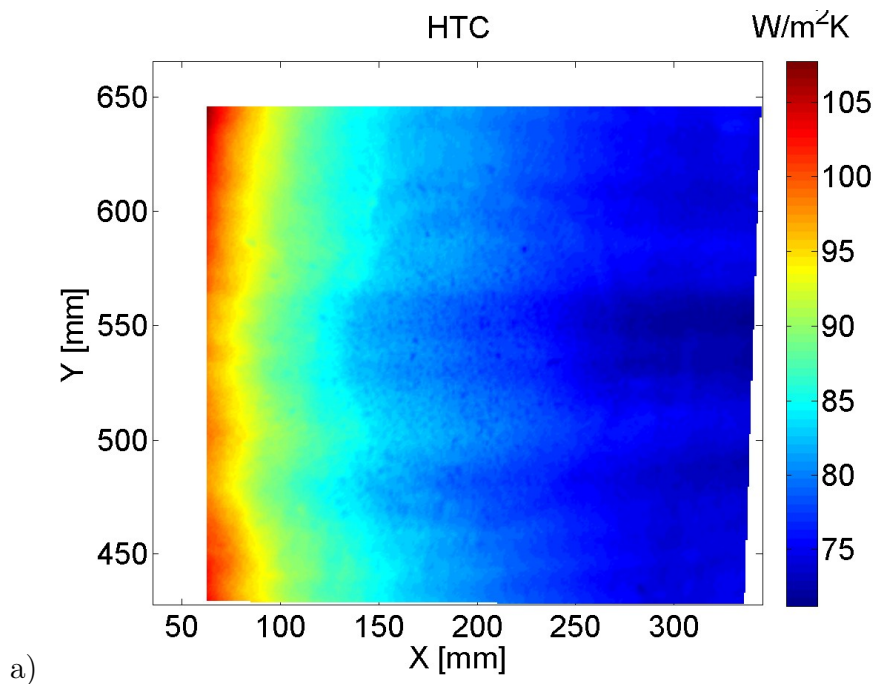
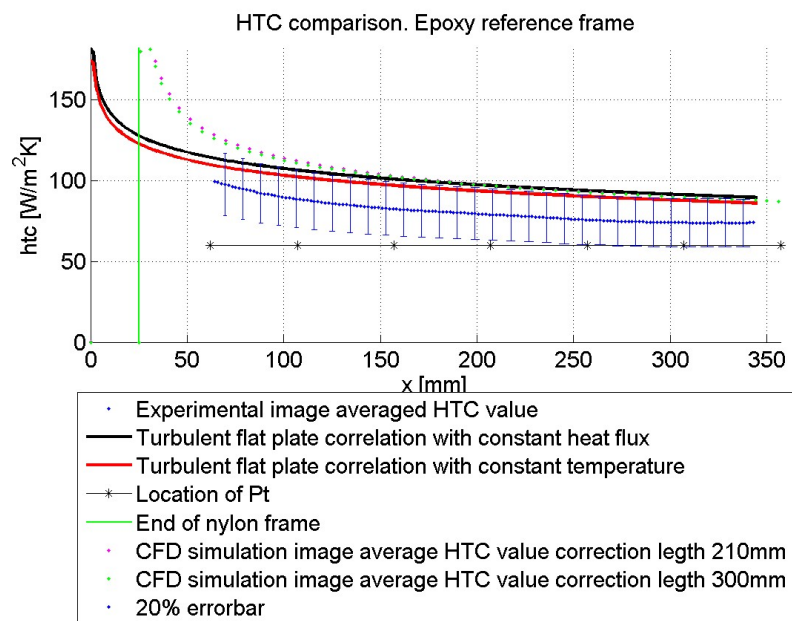


Figure 6.8: a) *HTC* at 25 m/s color map b) Averaged *HTC* at 25 m/s



a)



b)

Figure 6.9: a) *HTC* at 30 m/s color map b) Averaged *HTC* at 30 m/s

In Fig. 6.7 , 6.8 and 6.9, the green line represents where the nylon ends. This

line is drawn to check the effects of the contact between the aluminium and the frame made of nylon.

The red and the black line are the HTC taken as reference for the validation, calculated through Eq. 1 and 2 respectively. The assumptions are:

- Constant heat flux for the black line.
- Constant temperature for the surface for the red line.

The blue line, represent at the different velocity cases, represents the average value of the HTC height-wise. In addition, CFD simulations are carried out in Fluent for this case. Two different virtual distances are studied in order to understand the effect of the unheated starting length. Although the obtained HTC values are within the guidelines established by the theory, when the error is applied, in the illustrations it is observable that the endwall presents an offset so that the blue lines are always below the red and the black one.

This observed shift is due to the fact that the manufacturer provides an estimated value of the thermal conductivity of $0.2 \frac{W}{mK}$, but without an interval error. Assuming, a 10% error of this value the relative error in the HTC would be around 17% (see Fig. 6.10 for relative errors) because of the uncertainty of this value. It is reasonable, that the thermal conductivity of the epoxy could be for example $0.22 \frac{W}{mK}$. Results assuming this value are shown in Fig 6.11.

According to Blair [13], although the equations of the 1 and 2 are suitable for most engineering calculations, in practice they rarely provide exact values for the convection coefficients. Conditions vary according to free stream turbulence and surface roughness, and errors as large as 25% may be incurred by using the expressions.

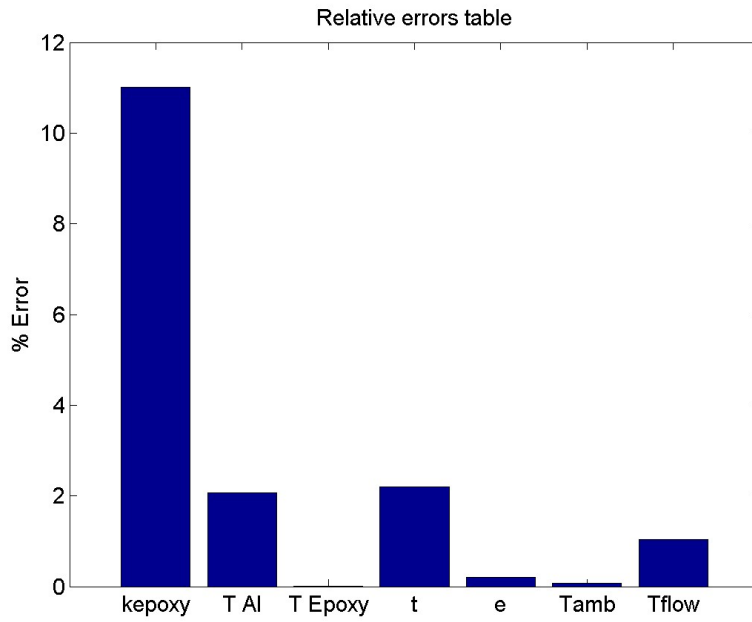


Figure 6.10: Percentage of error of all the parameters to calculate the HTC

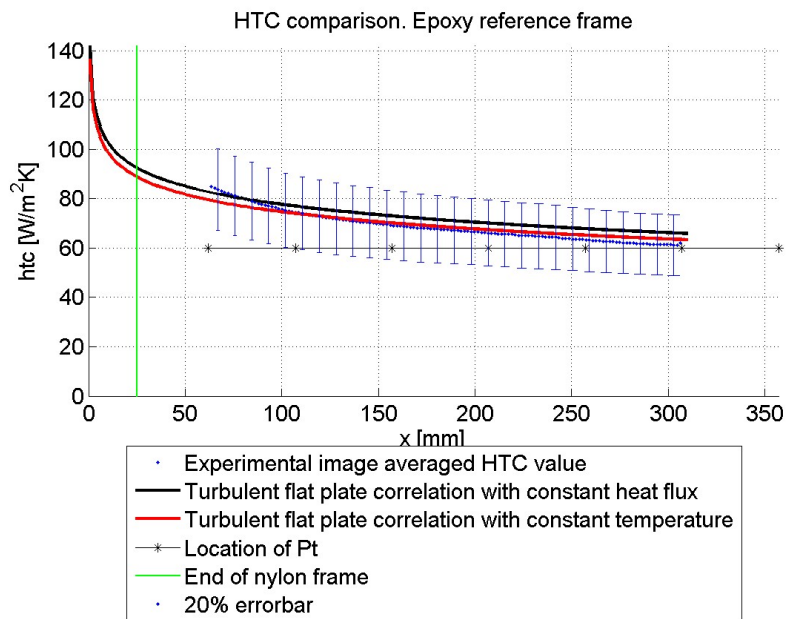


Figure 6.11: HTC at 20 m/s with $k_{epoxy} = 0.22 \frac{W}{mK}$

6.3 OGV cascade case

One of the aims of the Master thesis is the understanding of the heat transfer between the air flow and the wall when the OGVs have been installed in the linear cascade. To obtain the visualization of the air flow around one of the four vanes it was required to take two pictures, above and below of a reference vane. The shape of the vane immersed in the air flow can be seen in the Fig. 6.12

The upper and lower path heat transfer coefficient distribution are shown together in Fig. 6.12.

The measurement procedure and data post processing of the temperatures in the aluminum and epoxy surfaces are the same than for the case of flat plate. The Fluent simulations, supplied by Borja Rojo, solve the complete 3D problem resulting the heat transfer in the three directions. Afterwards, the upper and down simulations are joined by Matlab obtaining the results shown in Fig. 6.12.

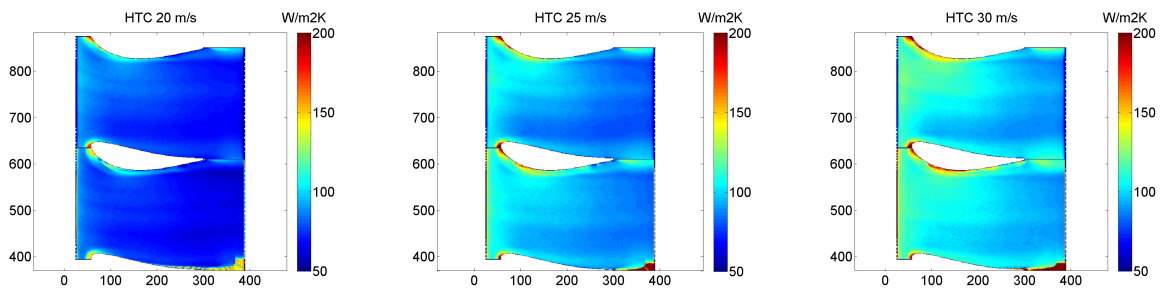


Figure 6.12: Convection heat transfer coefficient of the OGV. Left: **20 m/s** Central: **25 m/s** Right: **30 m/s**

Figure 6.12 shows how the value of the HTC increases with the speed, as it was expected. Furthermore, it is important to point out that from these results, the HTC on the upper path is around 2% lower than in the lower path, although the general behaviour of the flow is periodic. The highest values of the HTC founded at the most turbulent areas, the leading edge and trading edge.

The curvature in the trajectory of the fluid are consequence of the grid placed upstreams. The effect of the grids in the linear cascade has been studied [12] concluding that the grid does not affect adversely the flow and transport processes, however the vortex of the grid can be guessed from the images. The grid makes the flow more turbulent, as can be noted in the increase of the values of the HTC if they are compared with the flat plate. If figures for flat plate and OGV case are compared per each velocity the HTC increases around by 20%.

Chapter 7

Conclusions

The main conclusion of this Master thesis is that endwall built for the linear cascade has been validated successfully and the measures carried out in the linear cascade values fit with the theoretical correlations, taking as reference the Incropera [11]. When the flow immerses the entire endwall, the heat transfer coefficient is distributed without shape changes and the epoxy-aluminium interface temperature map can be obtained with the 21 Pt 100. This scenario is not the case of the jet impingement experiment. Therefore, a reason why the heat transfer coefficient results of the endwall in this case were inconclusive.

The methodology and measurement technique used is very accurate resulting the convection heat transfer coefficient with an error down to 20%, when the value of the epoxy's thermal conductivity material is known. The approximation made following the theoretical model (calculating the heat transfer in one direction), is proved to be very similar to the numerical results obtained from CFD software (Fluent), supplied by Borja Rojo. The advantage of the technique of the IR camera visualization gives more information in the images to discern the heat transfer around the vanes, mainly in the leading edge and the trailing edge. The mesh required to obtain the same quality than the camera (67.000 points) should be around 100 million of nodes. The hardware and the time required to design and compute this mesh highlighted the value of using this method instead.

Referring to the measurements on the OGV, the convection heat transfer coefficient obtained is about $70W/m^2K$, expected value if the results are compared with the convection heat transfer coefficient obtained by Carlos Jimenez [5]. Also the areas with higher HTC values correspond to the interaction between the vane and the wall as it was expected following previous research carried out in the linear cascade [5].

It is concluded that the endwall and all the set up for the linear cascade is ready to carry out different types of configurations of the endwall and vanes, changing for example the incident angle to the OGV or the characteristics of

the flow. Furthermore, the IR camera measurement technique is ready for future experiments. The data acquired in those experiments would be used for the backup obtained from CFD simulations.

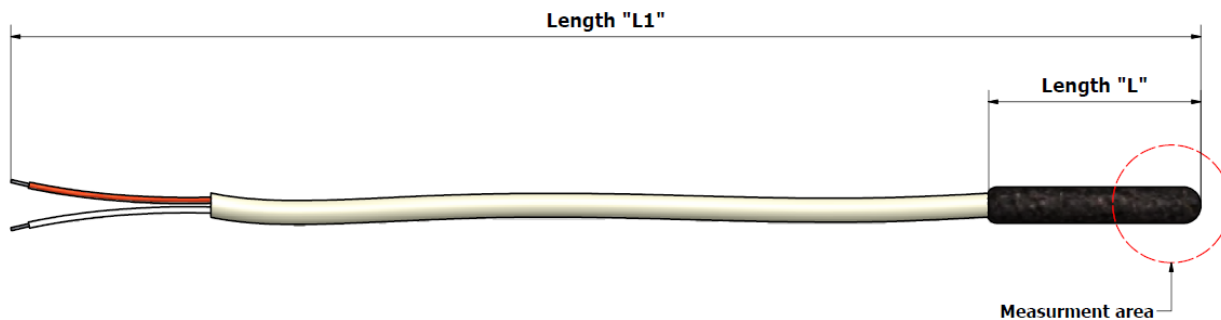
Chapter 8

Future work

The results obtained in this Master thesis for the heat transfer coefficient in the OGV belong to the on-design configuration. A future work could study the behaviour of the air flow for different inlet angles to the OGVs. Some improvements for the air measurements could be done in the linear cascade. For example, to get more accurate pressure measurements a Pitot tube could be installed before the bellmouth. It would lead to a more accurate calibration of the test area. Changing the acrylic window panel with windows for a transparent material for the IR-camera would be another improvement that could be included if the cost would not pose a problem. In addition other aero-measurement techniques can provide a better understanding of the flow inside the OGV cascade, such as hot wire anemometry or PIV (particle image velocimetry). Finally the HTC measurements will be compared with the results obtained by a research group from Lund University of Technology that studies the same case with a different experimental set up and measurement technique (thermochromic liquid crystals).

Data sheet

PS



PT1000 THERMIC ELEMENT WITH CABLE AND OVERMOULDED TIP

RANGE :

- -20°C / +100°C

USE :

- Universal

KEY POINT :

- Flexible

SPECIFICATIONS :

- PT100Ω thermic element A Class – 1x3 wires
- Overmoulded tip
- Cable 2 conductors, section 0.22mm, isolated PVC/PVC

DIMENSIONS :

- Tip length = 50mm
- Tip diameter = 6mm
- Total length (tip + cable) = 2000mm

METROLOGICAL DATA :

- As per IEC 751
- Standard tolerance PT100 A class :±0.15 + 0.002.[t°C]

Other dimensions:

TIP Diameter	6mm	8mm
Sensing element		
PT100Ω	370-6587	
PT1000Ω	547-7297	
Thermistance	-	370-6133

NEXTEL®

Suede-Coating 3101

7. Trade names	Base Material Hardener Thinner	NEXTEL-Suede-Coating 3101 NEXTEL-Härter 6018 NEXTEL-Verdünner 8061 NEXTEL-Verdünner 901-68 ALEXIT-Verdünner 901-26
8. Mixing ratio	8 parts by weight / volume 1 part by weight / volume	NEXTEL-Suede-Coating NEXTEL-Härter
9. Application	Compressed air spraying Efflux time (DIN 53211) Nozzle size Pressure	10 to 15 % Thinner 8061 / 901-68 or 20 to 25 % Thinner 901-26 40 to 60 seconds 1 to 1.8 mm 3 to 4 bar
	Processing at room temperatures of 20 to 25 °C and a relative humidity of 50 to 65 %: use Thinners 8061 and 901-68. Processing at room temperatures of 25 to 35 °C and a relative humidity of 50 to 65 %: use Thinner 901-26.	
10. Pot life	Room temperature	4 to 6 hours
11. Drying	Room temperature	dust-dry : 15 to 30 min touch-dry : 2 to 3 hrs
	Oven drying	10 to 25 minutes flash-off 30 to 40 minutes at 80 °C
	The drying parameters are selected in coordination with the specific purpose of the object to be coated.	
12. Packaging	NEXTEL-Suede-Coating 3101 including NEXTEL-Härter 6018 NEXTEL-Verdünner 8061 NEXTEL-Verdünner 901-68 ALEXIT-Verdünner 901-26	1 l, 5 l, 20 l net 1 l, 5 l, 20 l 5 kg, 25 kg net 5 kg, 25 kg net

Model Code (continued)

Code Description	Code Option	Option Description						
VI. Materials of Construction		Meter Type	Fitting	O-ring	Side Plates	Connection	In	Out
	V	FV retrofit	316SS	Viton	Stainless Steel Rugged	Flanged	Horizontal	Horizontal
	W	FV retrofit	316SS	Viton	Stainless Steel Rugged	Flanged	Vertical	Vertical
	X	FV retrofit	316SS	Viton	Stainless Steel Rugged	Flanged	Horizontal	Vertical
	Y	FV retrofit	316SS	Viton	Stainless Steel Rugged	Flanged	Vertical	Horizontal
	Z	FV retrofit	316SS	Kalrez	Stainless Steel Rugged	NPT	Horizontal	Horizontal
	1	FV retrofit	316SS	Kalrez	Stainless Steel Rugged	NPT	Vertical	Vertical
	2	FV retrofit	316SS	Kalrez	Stainless Steel Rugged	NPT	Horizontal	Vertical
	3	FV retrofit	316SS	Kalrez	Stainless Steel Rugged	NPT	Vertical	Horizontal
	4	FV retrofit	316SS	Kalrez	Stainless Steel Rugged	Flanged	Horizontal	Horizontal
	5	FV retrofit	316SS	Kalrez	Stainless Steel Rugged	Flanged	Vertical	Vertical
6	FV retrofit	316SS	Kalrez	Stainless Steel Rugged	Flanged	Horizontal	Vertical	
7	FV retrofit	316SS	Kalrez	Stainless Steel Rugged	Flanged	Vertical	Horizontal	
VII. Accessories	A	None						
	B	Inlet/Outlet left or right						
	C	Dual Scales						
	D	Inlet/Outlet left or right & Dual Scales						
	E	Dual Scales and front of panel mounting screws						
	F	Front of panel mounting screws						
	G	Inlet/Outlet left or right & Dual Scales & front of panel mounting screws						

Sample Standard Model Code

I	II	III	IV	V	VI	VII
1307F	J2	2	C	A1	A	A

Model 1307 - Approximate Shipping Weight (lbs./KG)

Meter Size	Threaded	Flanged
8, 10	7/3.1	8/3.6
12	8/3.6	18/8.2

Brooks Service and Support

Brooks is committed to assuring all of our customers receive the ideal flow solution for their application, along with outstanding service and support to back it up. We operate first class repair facilities located around the world to provide rapid response and support. Each location utilizes primary standard calibration equipment to ensure accuracy and reliability for repairs and recalibration and is certified by our local Weights and Measures Authorities and traceable to the relevant International Standards. Visit www.BrooksInstrument.com to locate the service location nearest to you.

START-UP SERVICE AND IN-SITU CALIBRATION

Brooks Instrument can provide start-up service prior to operation when required. For some process applications, where ISO-9001 Quality Certification is important, it is mandatory to verify and/or (re)calibrate the products periodically. In many cases this service can be provided under in-situ conditions, and the results will be traceable to the relevant international quality standards.

CUSTOMER SEMINARS AND TRAINING

Brooks Instrument can provide customer seminars and dedicated training to engineers, end users, and maintenance persons. Please contact your nearest sales representative for more details.

HELP DESK

In case you need technical assistance:

Americas ☎ 1 888 554 FLOW Europe ☎ +31 (0) 318 549 290 Asia ☎ +81 3 (0) 5633 7100

Due to Brooks Instrument's commitment to continuous improvement of our products, all specifications are subject to change without notice.

TRADEMARKS

Brooks Brooks Instrument, LLC
 Full-View Brooks Instrument, LLC
 Kalrez perfluoroelastomers DuPont Performance Elastomers
 Viton fluoroelastomers DuPont Performance Elastomers



Brooks Instrument
 407 West Vine Street
 P.O. Box 903
 Hatfield, PA 19440-0903 USA
 T (215) 362 3700
 F (215) 362 3745
 E-Mail BrooksAm@BrooksInstrument.com
www.BrooksInstrument.com

Brooks Instrument
 Neonstraat 3
 6718 WX Ede, Netherlands
 T +31 (0) 318 549 300
 F +31 (0) 318 549 309
 E-Mail BrooksEu@BrooksInstrument.com

Brooks Instrument
 1-4-4 Kitasuna Koto-Ku
 Tokyo, 136-0073 Japan
 T +81 (0) 3 5633 7100
 F +81 (0) 3 5633 7101
 E-Mail BrooksAs@BrooksInstrument.com

BROOKS
 INSTRUMENT

Bibliography

- [1] Low-speed Wind Tunnel testing, B.Barlow, H.Rae,Pope, Wiley-Interscience
- [2] C. Arroyo Osso, (2009) "*Aerothermal Investigation of an Intermediate Duct*", Thesis for the Degree of Doctor of Philosophy, Chalmers University of Technology.
- [3] Bradley M. Ratliff , Majeed M. Hayat and Russell C. Hardie, (2002) "*An algebraic algorithm for nonuniformity correction in focal-plane arrays* ", Optical Society of America, University of Dayton and University of New Mexico.
- [4] Azwitamisi E Mudau, Cornelius J Willers, Derek Griffith and Francois P J le Roux. "*Non-Uniformity Correction and Bad Pixel Replacement on LWIR and MWIR Images*", Defense, Peace, Safety and Security Council for Scientific and Industrial Research, CSIR Pretoria, South Africa
- [5] Carlos Jimenez (2013) "*Experimental Heat Transfer Studies with infrared camera*", Master's Thesis in Solid & Fluid Mechanics, Chalmers University of Technology
- [6] Saul Josep Llacer (2014) "*Instrumented window design and OGV air measurements*", Master's Thesis in Solid & Fluid Mechanics, Chalmers University of Technology, Göteborg, Sweden.
- [7] Hjarne, J., (2007) "*Turbine outlet guide vane flows*", PhD thesis, Chalmers University of Technology, Göteborg, Sweden.
- [8] Lei Wang, Bengt Sunden, Valery Chernoray, Hans Abrahamsson (2012) "*Experimental Heat Transfer Study of Endwall in a linear cascade*",Chalmers University of Technology, Göteborg, Sweden.
- [9] Vadiraj Katti, S.V. Prabhu (2007) "*Experimental study and theoretical analysis of local heat transfer distribution between smooth flat surface and impinging air jet from a circular straight pipe nozzle*",Department of Mechanical Engineering, Indian Institute of Technology, Bombay, Powai, Mumbai 400 076, India

-
- [10] Angel Barrachina Martin (2014) "*Heat transfer studies with an IR camera Thermography Techniques*", Chalmers University of Technology, Göteborg, Sweden.
- [11] Incropera, DeWitt, Bergman, Lavine (2007) "*Fundamentals of Heat and Mass Transfer*", 6th edition.
- [12] Volker Kottke "*Effects of screens and Grids on Nominally Two Dimensional Boundary layer* ", Institut für Chemische Verfahrenstechnik, Universität Stuttgart
- [13] M. F. Blair, (1938) "*Influence of Free Stream Turbulence on Turbulent Boundary Layer Heat Transfer and Mean Profile Development, Part I Experimental Data*", United Technologies Research Center, East Hartford.
- [14] Borja Rojo, Carlos Jimenez and Valery Chernoray (2013) "*Experimental Heat Transfer Study of Endwall in a linear cascade with IR Thermography*", Chalmers university, Göteborg, Sweden.
- [15] K. Jambunathan, E. Lai, M. A. Moss* and B. L. Button "*A review of heat transfer data for single circular jet impingement*", Department of Mechanical Engineering, Nottingham Polytechnic, Nottingham, UK.
- [16] Diaz, Rodrigo Andres Reeves. (2002) "*Compensacion de Ruido Espacial en Sistemas de Imagenes con Sensores Infrarrojos*", Universidad de Concepcion, Facultad de Ingenieria, Chile.